

A SELF-SUSTAINING, BOUNDARY-LAYER-ADAPTED  
SYSTEM FOR TERRAIN EXPLORATION  
AND ENVIRONMENTAL SAMPLING

Michael Morrow

Thesis submitted to the Faculty of the  
Virginia Polytechnic Institute and State University  
In partial fulfillment of the requirements for the degree of

Master of Science  
in  
Aerospace Engineering

Dr. C. A. Woolsey, Chair  
Dr. W. Mason  
Dr. H. Schaub

June 10, 2005  
Blacksburg, Virginia

Keywords: buoyancy-driven gliding, terrain exploration, Titan  
inboard wing, internal actuation, boundary layer

© 2005 Michael Morrow

Abstract

A SELF-SUSTAINING, BOUNDARY-LAYER-ADAPTED  
SYSTEM FOR TERRAIN EXPLORATION  
AND ENVIRONMENTAL SAMPLING

Michael Morrow

This thesis describes the preliminary design of a system for remote terrain exploration and environmental sampling on worlds with dense atmospheres. The motivation for the system is to provide a platform for long-term scientific studies of these celestial bodies. The proposed system consists of three main components: a buoyancy-driven glider, designed to operate at low altitude; a tethered energy harvester, extracting wind energy at high altitudes; and a base station to recharge the gliders. This system is self-sustaining, extracting energy from the planetary boundary layer.

A nine degree of freedom vehicle dynamic model has been developed for the buoyancy-driven glider. This model was used to illustrate anecdotal evidence of the stability and controllability of the system. A representative system was simulated to examine the energy harvesting concept.

# Acknowledgements

I would like to thank my advisor Craig Woolsey for the opportunity to participate in this novel research, and his guidance and patience throughout the entire process. I would like to thank my parents, Tim and Kathy Morrow, for supporting me in my endeavors and always believing in me. I would also like to thank Katie Scully; without her love and support, I could not have completed this work. I would also like to thank the Count, for starting me on this path, with his unending love of numbers. I would also like to thank my coworkers at Software Technologies Laboratory: Kris Schneider and Jonathan Pratt, for their constant humor. On the same note, I would like to thank my roommates Brian Evans, Brian Fleming, Chris Guglielmo, and Pat Butler for their friendship and constant joking. Last, I would like to thank all the members of my lab group: Amy Linklater, Chris Nickell, and Konda Reddy for assisting me whenever asked.

# Contents

<b>Abstract</b>	<b>ii</b>
<b>Acknowledgements</b>	<b>iii</b>
<b>Nomenclature</b>	<b>vii</b>
<b>1 Introduction</b>	<b>1</b>
<b>2 System Description</b>	<b>3</b>
2.1 Historical Perspective . . . . .	3
2.1.1 Venus - Venera landers, VEGA balloons, and Pioneer descent probes	3
2.1.2 Mars - Viking landers and three rovers . . . . .	4
2.1.3 Titan - Huygens descent probe . . . . .	5
2.2 Representative Environments . . . . .	5
2.3 Overview of System Architecture . . . . .	6
2.4 Revolutionary Aspects of System . . . . .	7
2.4.1 Internal actuation / Aerodynamic shape control . . . . .	7
2.4.2 Buoyancy-driven gliding flight . . . . .	9
2.4.3 Energy efficient motion . . . . .	9
2.4.4 Energy extraction . . . . .	10
<b>3 Titan Mission Concept Development</b>	<b>11</b>
3.1 Science Scenario . . . . .	11
3.2 Operating Environment . . . . .	12
3.2.1 Atmospheric boundary layer structure . . . . .	12

3.2.2	Wind regimes and climatology . . . . .	13
3.2.3	Surface characteristics . . . . .	16
<b>4</b>	<b>Low-Altitude Robotic Soarer</b>	<b>17</b>
4.1	System requirements . . . . .	17
4.1.1	Payload . . . . .	17
4.1.2	Survey altitude and speed . . . . .	17
4.1.3	Loitering and hovering . . . . .	18
4.2	Technology Overview . . . . .	18
4.2.1	Buoyancy-driven gliding flight . . . . .	18
4.2.2	Aerodynamic shape control . . . . .	21
4.2.3	Autonomous Dynamic Soaring . . . . .	22
4.3	Concept Development . . . . .	23
4.3.1	Mass . . . . .	23
4.3.2	Volume . . . . .	24
4.3.3	Lung capacity . . . . .	25
4.3.4	Chord length . . . . .	25
4.3.5	Aerodynamics . . . . .	26
4.3.6	Representative example . . . . .	31
4.4	Dynamic model . . . . .	32
4.4.1	Vehicle dynamics . . . . .	32
4.4.2	Equilibrium . . . . .	37
4.5	Future Development . . . . .	42
<b>5</b>	<b>Wind Energy Absorber</b>	<b>44</b>

5.1	System description . . . . .	44
5.2	Representative system . . . . .	44
5.3	Simulation . . . . .	45
5.4	Future Development . . . . .	46
<b>6</b>	<b>Extendibility to Other Operating Environments</b>	<b>47</b>
6.1	Venus . . . . .	47
6.2	Earth Hydrosphere . . . . .	48
6.3	Earth Atmosphere . . . . .	48
6.4	Europa . . . . .	49
<b>7</b>	<b>Conclusions</b>	<b>51</b>
	<b>References</b>	<b>54</b>
	<b>Abstract A: SCALARS Simulation Code</b>	<b>55</b>
	Simulation Setup . . . . .	55
	Simulation Code . . . . .	59
	<b>Vita</b>	<b>68</b>

# Nomenclature

$\hat{\cdot}$ = cross-product equivalent matrix	$\mathbf{r}_p$ = relative particle position (m)
$\mathbf{0}$ = column vector of 3 zeros	$r_{p1} = \mathbf{e}_1 \cdot \mathbf{r}_p$
$\mathbb{I}_{3 \times 3}$ = $3 \times 3$ identity matrix	$\mathbf{r}_{cg}$ = body center of gravity (m)
$AR$ = inboard wing aspect ratio: $AR = \frac{b^2}{S}$	$\mathcal{R}$ = body to inertial rotation matrix
$b$ = inboard wing span (m)	$S$ = inboard wing area (m <sup>2</sup> )
$\mathbf{b}_i = i^{\text{th}}$ basis vector for body frame	$S_H$ = horizontal stabilizer area (m <sup>2</sup> )
$c$ = inboard wing chord length (m)	$S_V$ = vertical stabilizer area (m <sup>2</sup> )
$\mathbf{C}_f$ = hydrodynamic coupling matrix (kg-m)	$T$ = kinetic energy (J)
$D$ = outboard hull diameter (m)	$\mathbf{v}_p$ = particle velocity (m/s)
$\mathcal{D}$ = drag force (N)	$v_{p1} = \mathbf{e}_1 \cdot \mathbf{v}_p$
$\mathbf{e}_i = i^{\text{th}}$ basis vector for $\mathbb{R}^3$	$\mathbf{v}$ = body translational velocity (m/s)
$f$ = outboard hull fineness ratio: $f = \frac{D}{L}$	$\mathbb{V}$ = total, nominal displaced volume (m <sup>3</sup> )
$\mathbf{f}$ = external force (N)	$\mathbf{X}$ = inertial position of body origin (m)
$g$ = local acceleration due to gravity (m/s <sup>2</sup> )	$\mathbf{X}_p$ = inertial position of particle (m)
$\mathbf{h}$ = body angular momentum (kg-m <sup>2</sup> /s)	$\eta$ = ratio of buoyancy lung capacity to $\mathbb{V}$
$\mathbb{I}$ = generalized inertia	$\boldsymbol{\eta}$ = generalized velocity
$\mathbf{I}_i = i^{\text{th}}$ basis vector for inertial frame	$\boldsymbol{\nu}$ = generalized momentum
$\mathbf{J}_b$ = rigid body inertia (kg-m <sup>2</sup> )	$\boldsymbol{\omega}$ = body angular velocity (rad/s)
$\mathbf{J}_f$ = added inertia (kg-m <sup>2</sup> )	
$L$ = outboard hull length (m)	<i>Subscripts</i>
$\mathcal{L}$ = lift force (N)	b = rigid body
$m$ = total vehicle mass (kg)	b/f = rigid body/fluid system
$m_b$ = mass of body (kg)	b/p = rigid body/mass particle system
$m_p$ = mass of particle (kg)	f = fluid
$\mathbf{m}$ = external moment (N m)	p = mass particle
$\mathbf{M}_f$ = added mass matrix (kg)	sys = rigid body/fluid/mass particle system
$\mathbf{p}$ = translational momentum (kg-m/s)	

# List of Figures

1	The Mars rovers Sojourner and Spirit/Opportunity. (Image credit: NASA/JPL)	4
2	System on Titan [5]. (Background credit: M. Messerotti)	7
3	System Components and the PBL [5].	8
4	Images of Titan’s surface by Huygens probe (Image credit: NASA/ESA/University of Arizona.)	12
5	Planetary boundary layer velocity profile	13
6	Atmospheric properties of Titan below 10 kilometers [5].	15
7	Diagram of the autonomous underwater glider “Spray” [22].	19
8	The four cross sections examined in [12]. From top to bottom: a “fat” ellipsoid, a “slender” ellipsoid, a cylinder with rounded ends (WRC Slocum), and a laminar flow body (UW/APL Seaglider). (Image credit: Russ Davis.)	20
9	Measured drag of four bodies as examined in [12]. The solid line is the measured drag curve from a test using the full scale UW/APL Seaglider model. (Image credit: Russ Davis.)	21
10	Diagram of the autonomous underwater glider “Slocum” [22].	22
11	SCALARS Initial Concept, left, and Refined Concept, right.	23
12	SCALARS internal components.	24
13	Hull length and diameter versus fineness ratio for $m = 10$ kg [5].	26
14	Vehicle lift coefficient versus angle of attack [5].	29
15	Vehicle drag coefficient versus angle of attack [5].	30
16	Glide angle versus angle of attack.	31
17	Glide angle versus angle of attack: $AR = 2$ and $b = \frac{3}{4}L$ [5].	33
18	Illustration of reference frames and notation for SCALARS vehicle model [5].	34
19	Angles in the plane of symmetry.	38

20	Flight path of SCALARS vehicle in a descending 180 degree left hand turn. .	41
21	Flight path of SCALARS vehicle for two ascending right hand turns. The top image is of a 90 degree right hand turn. The bottom image shows a 180 degree right hand turn. . . . .	43
22	OAWEA internal components. . . . .	44
23	A two-stage towing system [5]. . . . .	45
24	A limit cycle oscillation in an unstable two-stage towing system. . . . .	45
25	Venus, as imaged by Galileo. (Image credit: NASA) . . . . .	47
26	Earth, as imaged by Galileo. (Image credit: NASA) . . . . .	49
27	Europa, as imaged by Galileo. (Image credit: NASA) . . . . .	49
28	A deep-sea hydrothermal vent (left, Image credit: NASA [30]) and a colony of tube-worms (right, Image credit: NASA [31]). . . . .	50

## List of Tables

1	Planetary Atmospheric Properties . . . . .	5
2	Comparison of specific power of various flyers (on Earth). . . . .	10
3	Wing parasite drag coefficient $C_{D_{wp}}$ versus Reynolds number and base area [5].	28

# 1 Introduction

Mankind has always been driven to explore the unknown. We have expanded our cumulative knowledge through the exploration of our world and observation of the universe around us. Our thirst for knowledge is seemingly endless, motivating technological advancement to fuel new discoveries.

The planets of our solar system have been a source of interest for thousands of years. Ancient civilizations erected temples and shrines in honor of these celestial bodies. The Egyptians erected pyramids to direct their pharaohs to the stars. The ruins of Stonehenge have been assumed to be a monument to the sun. The Greeks and Romans celebrated the celestial bodies through embodiment in their gods and goddesses. In more recent history, celestial mechanics inspired Copernicus, Kepler, Galileo, Newton, and many more scientists to form the mathematical foundation for modern physics.

Bodies with dense atmospheres have been particularly interesting, concealing their secrets behind a thick veil. Saturn's moon Titan and the planet Venus are two bodies which exhibit such a shroud. Studying the atmospheric processes on these bodies may reveal information about our own planet. Exploration of Titan's atmosphere, surface, and subsurface chemistry may also lead scientists to clues of the origins of life on Earth.

Recently, NASA has shown increased interest in exploration. This interest has been outlined through the visionary challenges pertaining to "Surface Exploration and Expeditions" [1]. These challenges are (quoting from [1]):

- Mobile Surface Systems. Highly robust, intelligent and long-range Mobile Systems to enable safe/reliable, affordable and effective human and robotic research, discovery and exploration in lunar, planetary and other venues.
- Flying and Swimming Systems. Highly effective and affordable Flying and Swimming systems to enable ambitious scientific (e.g., remotely operated sub-surface swimmers) and operational (e.g., regional overflight) goals to be realized by future human/robotic missions in lunar, planetary and other venues.
- Sustained Surface Exploration & Expeditions Campaign Architectures. Novel and robust architectures that best enable Sustained Surface Expeditions and Exploration

Campaigns to be undertaken to enable ambitious goals for future human/robotic research, discovery and exploration.

NASA Institute for Advanced Concepts (NIAC) sponsors the preliminary development of revolutionary ideas, such as novel planetary exploration systems. This thesis was completed under a six month exploratory research grant from NIAC. This thesis covers the preliminary design of a revolutionary system for planetary exploration of celestial bodies with dense atmospheres.

## 2 System Description

This section outlines the historical motivations for remote terrain exploration and environmental sampling on worlds with dense atmospheres, such as Titan and Venus. This section then provides an overview of a proposed system for planetary exploration. This system architecture was motivated as a response to visionary challenges enumerated by NASA's Office of Space Flight in regard to Surface Exploration and Expeditions, as presented in [1] and summarized in Section 1.

### 2.1 Historical Perspective

#### 2.1.1 Venus - Venera landers, VEGA balloons, and Pioneer descent probes

The Soviets were the first to attempt to send probes to Venus, with their Venera probes. The first probe that could be considered a success was the Venera 3, impacting the surface of Venus in March 1966. The next three attempts at exploring Venus, Venera 4 through 6, were unsuccessful in their missions. Undeterred, the Soviets continued sending probes to the mysterious planet, and finally made progress with the first successful data transmission from the surface of Venus by Venera 7 in December 1970, before the probe surrendered to the intense atmospheric conditions. The next success came from the Venera 9 and 10 probes; these probes took the first photographs of Venus's surface. The culmination of the Venera line of probes was the color photographs returned by Venera 13 and 14, and the mapping of the surface by Venera 15 and 16 [2].

Following the Venera projects, the Soviets embarked on the VEGA missions in 1985, which comprised three components: a lander, a balloon, and flyby probes for Halley's comet. The VEGA balloons drifted in the currents of the Venusian atmosphere, collecting data and sending it back to Earth [2].

In 1978, NASA responded to the Venera project by the Soviets with the Pioneer project. The Pioneer probes included an orbiting satellite and a spacecraft with three descent probes. These probes were released from the main spacecraft and descended to the surface, relaying more information about the atmosphere [2].

### 2.1.2 Mars - Viking landers and three rovers

Mars, as our nearest neighbor without an extremely corrosive atmosphere, has been visited by landers and three rovers. The first lander to successfully land on Mars was the Viking 1 in July 1976 [3]. In September of 1976, Viking 2 joined Viking 1 in the northern hemisphere of Mars. For six years, these two landers were able to analyze soil samples, inconclusively testing for life, and take over 4500 close-up images of the Martian surface [3].

The next major advancement of the exploration of Mars was the landing of the Sojourner rover in 1997. This vehicle was the first robot to explore another planet, by travelling roughly 100 meters. The Sojourner collected surface samples during the mission. In January 2004, the Spirit and Opportunity rovers landed on Mars. These more capable rovers have travelled a combined 7 kilometers, relaying imagery of the surface, including conclusive evidence that water once existed on Mars.



Figure 1: The Mars rovers Sojourner and Spirit/Opportunity. (Image credit: NASA/JPL)

The many successes of exploring Mars by probes and rovers motivates further exploration of other bodies in our solar system. However, there are limitations to the further application of rovers. Due to the use of wheeled locomotion, rovers were deployed in benign terrain. Areas of scientific interest may exist where rovers can not travel. Therefore, another method of transportation must be considered.

### 2.1.3 Titan - Huygens descent probe

Titan, the largest moon of Saturn, has been of interest to astronomers since it was discovered in 1655 [4]. Until imaged by Voyager 1 in 1981, Titan remained an enigma, hidden behind a shroud of a thick, smoggy atmosphere [5]. Recently, the Cassini orbiter was sent to Saturn, carrying the Huygens descent probe. The Cassini orbiter will continue to take images of Titan throughout its mission, while the Huygens probe provided new information and imagery from the surface of the moon. In [6], R. D. Lorenz classifies Titan as a cryogenically preserved organic chemistry lab, possibly containing a variety of prebiotic or protobiotic compounds which could influence opinion of the origins of life on Earth. This motivates further exploration of the recently unveiled moon.

## 2.2 Representative Environments

The system proposed in Section 2.3, while designed with exploration and investigation on Titan in mind, can be extended to nearly all fluid environments. Compared to Earth, Titan's atmosphere is four times as dense and the gravitational acceleration is approximately an order of magnitude smaller. In Table 1, some key properties of potential operating environments are listed.

Table 1: Planetary Atmospheric Properties

Property	Earth [7]	Venus [8]	Titan [4]	Earth Hydrosphere
Radius (km)	6378	6052	2575	6378
Mass (kg)	5.972e24	4.869e24	1.346e23	5.972e24
Surface Gravity (m/s <sup>2</sup> )	9.81	8.87	1.35	9.81
Surface Temperature (°C)	14	457	-179	-
Surface Density (kg/m <sup>3</sup> )	1.23	66.5	5.26	1027
Surface Pressure (bar)	1.01	94	1.44	-

## 2.3 Overview of System Architecture

The system outlined below is designed to be self-sustaining, extracting energy from the environment through exploitation of the planetary boundary layer. The system consists of three main components:

- **SCALARS (Shape Change Actuated, Low Altitude Robotic Soarers)**. These vehicles are rechargeable, autonomous, buoyancy-driven gliders actuated through internal shape control.
- **OAWEA (Oscillating-Aerofoil Wind Energy Absorber)**. This vehicle is tethered to the base station, operating at a higher altitude and extracting energy from the ambient flow. This device adjusts for optimal wind energy extraction through internal shape control.
- **Docking Station**. A docking station will inductively recharge the gliders, upload science data, and download revised mission commands.

The system is designed to exploit the planetary boundary layer. The OAWEA operates at high altitudes to extract energy, where the energy content is greatest, while the SCALARS expend the harvested energy at low altitude, where the conditions are more quiescent. This energy-harvesting theme is repeated by the SCALARS through the use of dynamic soaring. Energy for sustained flight is harvested exploiting the vertical wing gradient in the low atmosphere. The entire system is depicted on an artist's rendition of Titan in Figure 2, where the SCALARS vehicles are shaded blue, and the green OAWEA vehicle is tethered to the docking station.

The proposed system, as seen in Figure 3, can be extended to other fluid environments, including Titan's liquid hydrocarbon lakes (if these exist), the Venusian atmosphere, and the oceans of Earth. The extendibility of the system to these other environments will be discussed further in Section 6. This system, while novel, has roots in current technology and current topics of applied research. Thus, the enabling technologies required by the system should be available for application in the near future.

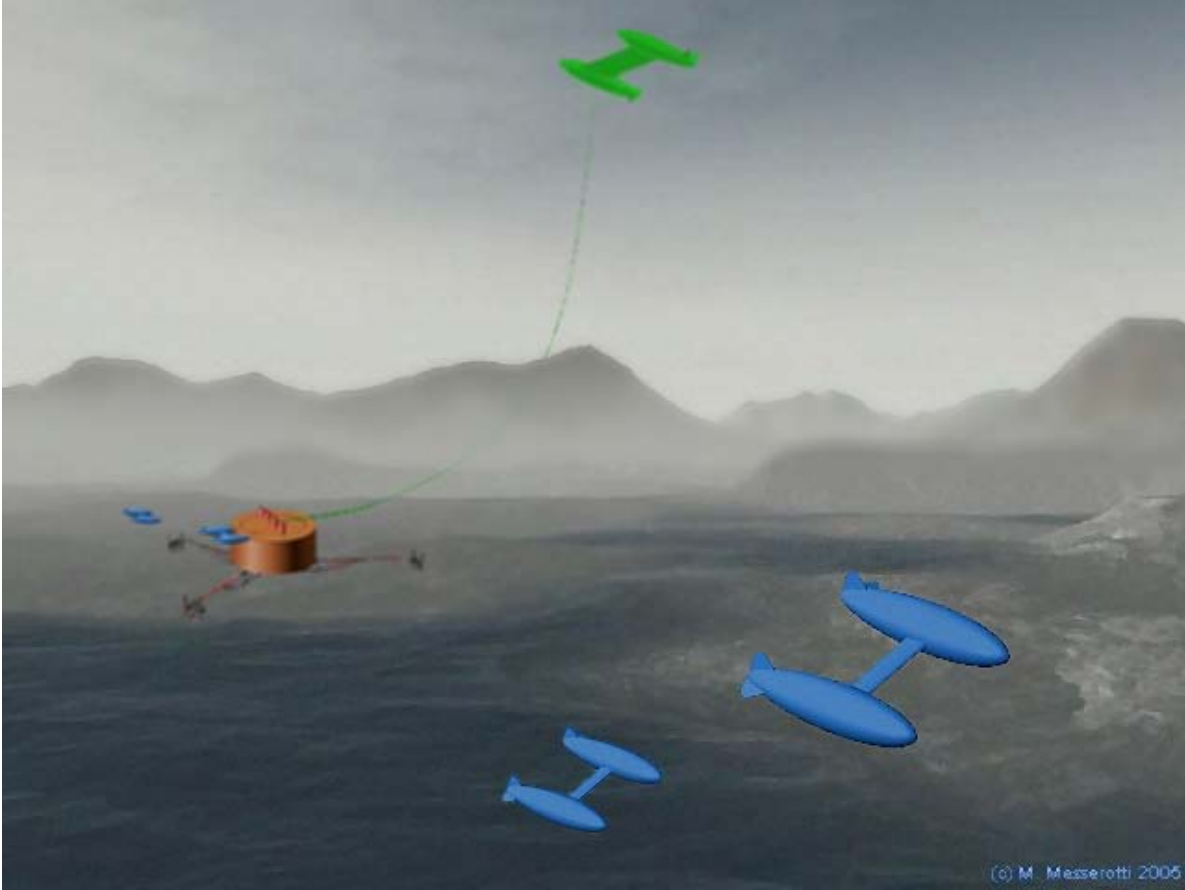


Figure 2: System on Titan [5]. (Background credit: M. Messerotti)

## 2.4 Revolutionary Aspects of System

The system features several ambitious concepts in response to the far reaching goals of the project. Internal actuation, aerodynamic shape control, buoyancy-driven gliding flight, energy efficient motion, and energy extraction distinguish this system from past exploration missions and concepts.

### 2.4.1 Internal actuation / Aerodynamic shape control

Currently, external actuation is typically used for lateral-directional control of unmanned autonomous vehicles, exposing key components to the environment. The proposed system is completely internally actuated, protecting the actuators and other vital components from

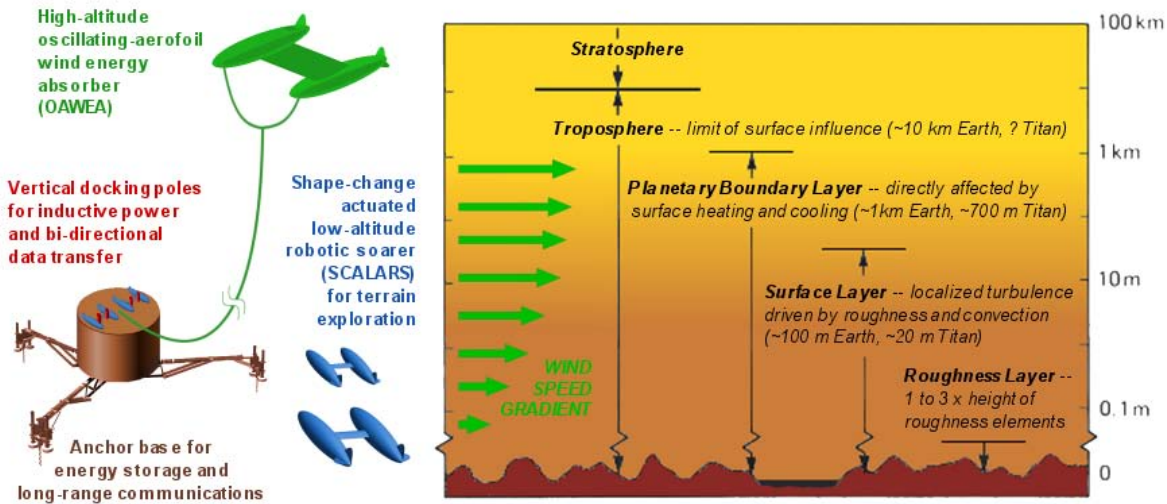


Figure 3: System Components and the PBL [5].

corrosion, dust, or other elements present in hostile environments. In order to facilitate lateral-directional control, the system features an elastic inboard-wing, twin-hull configuration.

The elastic inboard wing places the SCALARS vehicle in the category of morphing wing aircraft. With the advent of “smart materials”, morphing wing aircraft have garnered attention over the last decade. Morphing wing technologies are categorized as discrete or continuous, based on whether the shape change can be described by a finite number of parameters or not. Conventional hinged actuators and variable sweep actuators are examples of discrete morphing wing technologies. Continuous morphing wing technologies include conformal control surfaces, see [9] and [10]. These vehicles strive to obtain optimal performance through conformal deformation of the lifting surfaces.

The SCALARS design employs a continuous morphing technology similar to the Wright brothers’ “wing warping”, through asymmetric displacements of its mass actuators. The disparity between mass locations causes a torque on the wing, resulting in twisting of the elastic wing. This causes asymmetric loading on the wing, forming a rolling moment in a uniform flow. One concern with this form of roll control is that adverse yaw is also created. After rolling, the masses can be moved synchronously forward to counter the adverse yaw.

### 2.4.2 Buoyancy-driven gliding flight

Buoyancy-driven gliders have been successfully demonstrated in applications involving Earth's oceans. Long-term oceanographic monitoring has always been a desire of ocean scientists. Due to power storage limitations and inefficient propulsion for conventional vehicles, these observations have not been possible on the scale, or frequency, necessary to glean information on large-scale long-term natural phenomena. Conventional propeller-driven autonomous underwater vehicles (AUVs) are able to operate on a small time scale (on the order of one day), while the battery powered underwater gliders Seaglider [11] and Spray [12] can remain deployed for several weeks. The Thermal Slocum extends this operating time to nearly five years by exploiting the thermal stratification in the deep ocean [13]. These vehicles are reviewed in Section 4.2.

While buoyancy-driven gliding is not a new technology, most of the work has gone into developing working gliders, and very little work has been put into the fundamental analysis of the dynamics and control of these vehicles. Some preliminary work has been completed in [14], [15] and [16], but significant work remains if the technology is to be effectively adapted for use on Titan.

### 2.4.3 Energy efficient motion

People have long admired the ability of birds to travel over long distances, with what seems to be minimal effort. The wandering albatross [17] and other soaring birds are able to cover long distances by exploiting wind gradients. This clever use of a natural atmospheric feature is known as dynamic soaring. A comparison between various methods of locomotion can be seen in Table 2 [5]. A wandering albatross's specific power consumption is an order of magnitude smaller than conventional fixed wing aircraft and coaxial helicopters. Dynamic soaring creates this reduction in specific power consumption.

Dynamic soaring is distinct from static soaring commonly used by sailplane pilots and carrion birds. Static soaring uses the upward flow of air to move the vehicle further than could be done in static air. This flow can be created by natural geographic formations, such as a hill, or through the rise of warm air through the surrounding cooler air. These atmospheric flow features tend to be localized, and cannot be exploited for long distance exploration missions.

Table 2: Comparison of specific power of various flyers (on Earth).

Type of Flight Vehicle	Specific Power (Watts per kg)
Wandering albatross (with a mass of 10 kg at a ground speed of 11.7 m/s)	5.1
Lighter-than-air vehicle (at albatross mass and speed)	112
Fixed wing aircraft (at albatross mass and speed)	63
Coaxial helicopter (at albatross mass and speed); see [18]	75

Conversely, dynamic soaring makes use of a wind gradient, which exists anywhere there is a shear flow.

Dynamic soaring requires some demanding maneuvers. The vehicle begins with a slow descent with the flow, trading potential for kinetic energy. This increases the air-speed of the vehicle, due in part to the decreased wind speed within the lower part of the boundary layer. At the end of this glide, the vehicle turns into the wind, climbing quickly and trading this excess kinetic energy for altitude [19].

#### 2.4.4 Energy extraction

The energy extraction of the OAWEA vehicle and the energy efficient motion of the SCALARS vehicle work together to extend the duration of the individual vehicle missions, enabling more ambitious science objectives. The OAWEA employs inductive linear generator modules to extract energy from the motion of the vehicle. The linear generator modules comprise a permanent magnet suspended in a stator coil by springs. The springs are calibrated, based on the motion of the vehicle, to create resonance in the moving magnet. The passing of the permanent magnet through the stator coil creates a current which can charge ground based batteries to later replenish the SCALARS vehicles.

### 3 Titan Mission Concept Development

The exploration of Titan may provide information about the emergence of life on Earth. The cryogenic environment of Titan could be preserving a variety of prebiotic compounds [6], which may hold scientific significance for understanding the initial development of life. Titan is also the only other member of the solar system known to have liquid on its surface. The recent landing of the Huygens probe, and data from the Cassini orbiter increase the drive to further explore this enigmatic environment.

Titan provides an opportunity to improve our understanding of atmospheric mechanics and geophysics. Current exploration vehicles cannot operate over large spatial and temporal scales required. To meet large scale, long duration exploration requirements, the vehicle must be maneuverable without regard to the terrain. This is the key benefit of a buoyancy-driven glider over wheeled and tracked rovers.

The buoyancy-driven glider will be able to survey terrain inaccessible to ground based rovers. Figure 4 shows images of Titan's surface. The left image shows what appears to be a floodplain, which the Huygens probe revealed to have the consistency of wet clay or sand, with a thin, icy crust [5]. The two cobbles just below the middle of the image have an estimated width of 15 centimeters (flat one on the left) and 4 centimeters (rounded one with scoured base) [5]. The aerial view in the right image shows what appears to be a drainage field leading to a shore line. Rovers are unable to gather such data, and can be bogged down since the surface has the consistency of wet clay or sand. A buoyancy-driven glider will be capable of vertical take-off and landing without disturbing the sample site [5].

#### 3.1 Science Scenario

Representative science missions for exploring Titan have been identified to help define the scientific payload size and power requirements. These requirements, in turn, provide quantifiable boundaries for a number of system design parameters, including power generation and storage requirements for OAWEA and speed and maneuverability requirements for SCALARS. Once these requirements have been fixed, specific design optimization decisions can be made regarding the size and shape of the vehicle hull, the inboard wing and empen-

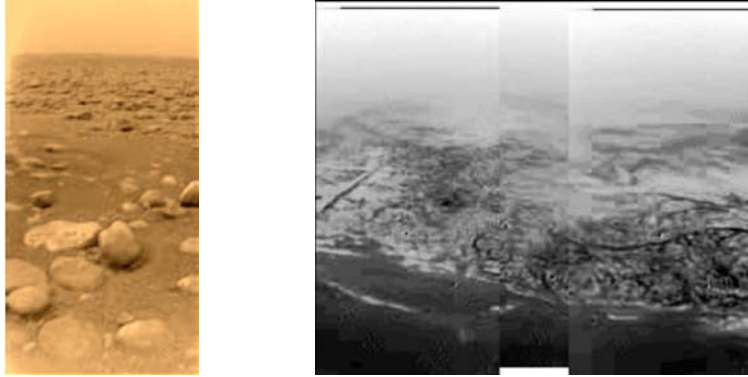


Figure 4: Images of Titan’s surface by Huygens probe (Image credit: NASA/ESA/University of Arizona.)

nage, the variable buoyancy actuator and the moving mass actuators. Following is a sample of Titan science missions which the proposed architecture could support.

- **Regional or global surface imaging, magnetometry, and gravity gradiometry.** These scientific objectives cannot be sufficiently covered by an orbiter due to resolution and atmospheric conditions. The proposed system can fulfill these goals because it pierces the atmosphere by flying at low altitudes.
- **Regional or global atmospheric sampling.** Titan provides an opportunity to improve our understanding of atmospheric mechanics and geophysics. Current exploration vehicles cannot sufficiently cover the large spatial and temporal scales required to fully investigate these topics.
- **Surface chemistry analysis.** The SCALARS vehicles will be able to take light duty samples of the surface through its vertical take off and landing capabilities.

## 3.2 Operating Environment

### 3.2.1 Atmospheric boundary layer structure

The planetary boundary layer exists as a result of tidally driven flows and the viscosity of the atmosphere. There exists a no slip condition on the surface of the planet, and the

velocity increases as the altitude increases. The velocity is dependent on the altitude and “free stream” velocity. The “free stream” is defined as the velocity where the flow is not in shear motion [20]. The planetary boundary layer velocity profile is depicted in Figure 5.

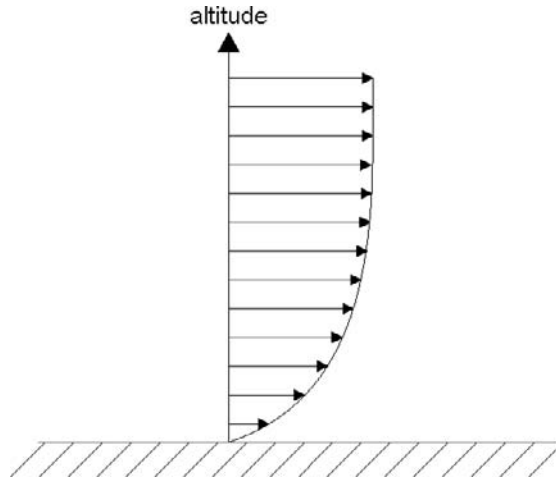


Figure 5: Planetary boundary layer velocity profile

### 3.2.2 Wind regimes and climatology

The winds on Titan are expected to be slow at the low altitudes where the SCALARS vehicle will operate. According to Lorenz, the winds will be on the order of one or two tenths of a meter per second [6]. The following atmospheric properties were computed according to approximations in Appendix A of [6].

**Temperature.** The temperature varies linearly with altitude in the low atmosphere (< 20 km). The temperature is described by the following equation:

$$T = T_0 - 1.15h \text{ K},$$

where  $h$  is altitude in kilometers, and  $T_0$  is approximately 94 K. Above 20 km, and below 100 km, the temperature increases to approximately 170 K, where it remains relatively constant.

**Density.** For altitudes between zero and forty kilometers, Lorenz suggests using the following equation for density:

$$\rho = 10^{[A+Bh+Ch^2+Dh^3+ Eh^4]} \text{ kg/m}^3,$$

where the coefficients are

$$\begin{aligned} A &= 0.72065 & B &= -1.28873 \times 10^{-2} \\ C &= -3.254 \times 10^{-4} & D &= 2.50104 \times 10^{-6} \\ E &= 6.43518 \times 10^{-5} \end{aligned}$$

**Pressure.** The pressure can be determined from the ideal gas law

$$P = \rho RT$$

where  $R$  is gas constant of the atmosphere,  $T$  is the temperature, and  $\rho$  is the density. The atmosphere on Titan consists of mostly nitrogen. Approximating the atmosphere as pure nitrogen, we have

$$R = \frac{\mathcal{R}}{m_{N_2}} = \frac{8.3144 \text{ J/mol K}}{28.01 \text{ g/mol}} \frac{1000 \text{ g}}{1 \text{ kg}} = 296.84 \frac{\text{N m}}{\text{kg K}}.$$

where  $\mathcal{R}$  is the universal gas constant, and  $m_{N_2}$  is the molecular mass of nitrogen.

**Viscosity.** Dynamic viscosity is given by the equation

$$\mu = 1.718 \times 10^{-5} + 5.1 \times 10^{-8}(T - 273) \text{ Pa s},$$

where the temperature  $T$  is given in Kelvins. Using the temperature at Titan's surface, the viscosity is found to be about  $8 \times 10^{-6}$  Pascal-seconds. This viscosity is roughly half that of Earth's atmosphere. (Note:  $\mu = \nu\rho$  where  $\nu$  is the kinematic viscosity.)

**Property Plot.** Figure 6 shows four principal properties from the surface of Titan to an altitude of 10 kilometers. From this figure, it is clear that these properties can be reasonably

assumed constant within the first 6 kilometers.

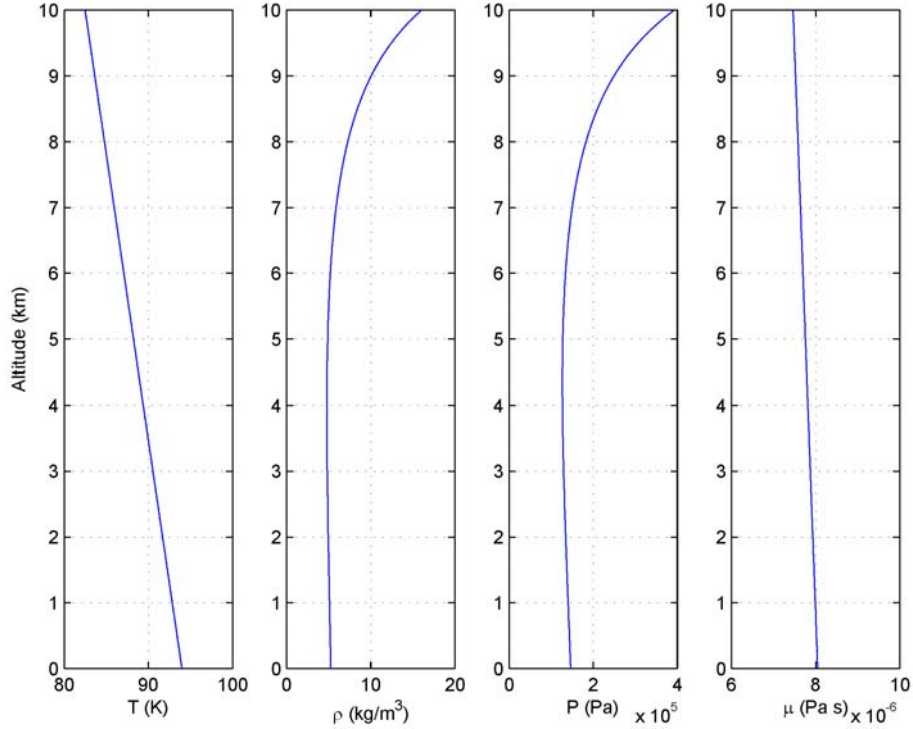


Figure 6: Atmospheric properties of Titan below 10 kilometers [5].

**Speed of Sound.** To determine the speed of sound, the atmosphere is again approximated as pure nitrogen. The specific heat of nitrogen at constant pressure is

$$c_p = 1.04 \frac{\text{J}}{\text{g K}}.$$

Given  $R$  for nitrogen, above, we compute

$$c_v = c_p - R = 0.74316 \frac{\text{J}}{\text{g K}}.$$

Thus, the ratio of specific heats is

$$\gamma = \frac{c_p}{c_v} = 1.40$$

The speed of sound, at the surface of Titan, can be calculated by

$$\begin{aligned} a &= \sqrt{\gamma RT} \\ &= \sqrt{(1.40) \left( 296.84 \frac{\text{N m}}{\text{kg K}} \right) (94 \text{ K})} \\ &= 197.6 \frac{\text{m}}{\text{s}}. \end{aligned}$$

### 3.2.3 Surface characteristics

While water only exists as a solid at the temperature and pressure on the surface of Titan, methane exists in three states; the temperature and pressure are near the triple point for methane. This fact leads scientists to speculate that the dark, river-like channels, which cut the terrain, are created by the flow of liquid methane. Like Earth, Titan likely experiences precipitation, but in the form of liquid methane as opposed to liquid water. This precipitation feeds the flow of methane through the channels, which creates the smooth appearance of the cobbles in Figure 4, as well as the scoured base seen below the center of the image.

The Huygens probe discovered the surface has the consistency of wet clay or sand, with a thin, icy crust. This surface typically has a layer of “crud” from photochemical reactions in the upper atmosphere, where some light from the sun is able to penetrate. This “crud” is speculated to be washed into the channels by the methane precipitation. This dynamic environment may prove problematic to rovers, where the a glider will have no issues, using variable ballast to land and take off as necessary to sample.

## 4 Low-Altitude Robotic Soarer

This section describes the Shape Change Actuated, Low Altitude Robotic Soarer (SCALARS).

### 4.1 System requirements

Our objective is to explore remote terrain and sample the environment on a global scale. For example, the vehicles must be able to overcome obstacles presented by the terrain and must be extremely efficient. These requirements motivate the configuration and design of SCALARS.

SCALARS will be required to operate in the cryogenic environment on Titan [4]. For example, the materials selected for the vehicle must be able to withstand the temperatures near the surface of below 100 K [4].

#### 4.1.1 Payload

The scientific instruments needed for terrain exploration and environmental sampling will be divided among the fleet of SCALARS. The division of instrumentation will reduce the mass of the individual SCALARS, and thus reduce the size. Each SCALARS will contain at least two science instruments, in addition to its guidance, navigation, and control instrumentation. Redundancy in instrumentation between the vehicles prevents failure of one vehicle from reducing the scientific effectiveness of the mission.

The SCALARS vehicles are designed to be 10kg, based on previous research on mission concepts and vehicles for terrain exploration of Titan [6, 21].

#### 4.1.2 Survey altitude and speed

SCALARS will operate at low altitudes on Titan, where the atmosphere is nearly quiescent. The expected winds at this altitude are on the order of one or two tenths of a meter per second [6]. Thus, the design speed of half a meter per second, as discussed in Section 4.3.3, will allow the SCALARS vehicle to make progress against the natural flow.

### 4.1.3 Loitering and hovering

In some scientific missions, it may be required for the SCALARS vehicle to loiter or hover over a location for an extended period of time. Because buoyancy driven vehicles can make progress against an atmospheric flow, the SCALARS vehicles will be able to fulfill this requirement.

## 4.2 Technology Overview

### 4.2.1 Buoyancy-driven gliding flight

Buoyant gliders are able to soar over the terrain, avoiding unknown terrain features. They are capable of vertical take-off and landing, enabling the sampling of terrain without disturbing the surrounding environment. These key features motivated the use of buoyancy-driven gliding flight on Titan.

The largest concern for long term terrain exploration is power consumption. Sensors need to be chosen so that they do not dramatically increase the power consumption, thus having little effect on mission duration. Sensors also must be chosen such that they do not significantly add to the drag of the vehicle. The three ocean gliders reviewed in this section have power consumption on the order of 1W.

**The Seaglider.** The Seaglider was designed for missions of one year over ocean-basin ranges. The Seaglider uses movement of internal masses to control pitch and roll. To control buoyancy, a high pressure reciprocating pump is used to move hydraulic fluid between internal and external bladders. To avoid pump failures, a separate boost pump is used [22].

To meet the one year endurance requirements, the Seaglider employs a low-drag laminar-flow shaped hull. According to [22], this design has a form drag proportional to  $V^{\frac{2}{3}}$  instead of the usual quadratic drag. This benefit is seen at higher velocities, as seen in Figure 9.

**The Spray.** The Spray was designed for long term missions that require the ability to move several thousand kilometers [12]. It utilizes GPS for location determination and ORBCOMM

satellite communication for data transfer.

The Spray’s pitch and roll control were implemented by moving a set of lateral battery packs, as seen in Figure 7. A centrally located, symmetric battery pack was used to control pitch. The second battery pack occupied approximately 180 degrees and could be rotated around the central column to control roll of the vehicle. These were both controlled through use of potentiometers for position determination and moved by DC motors driving rack-and-pinion actuators.

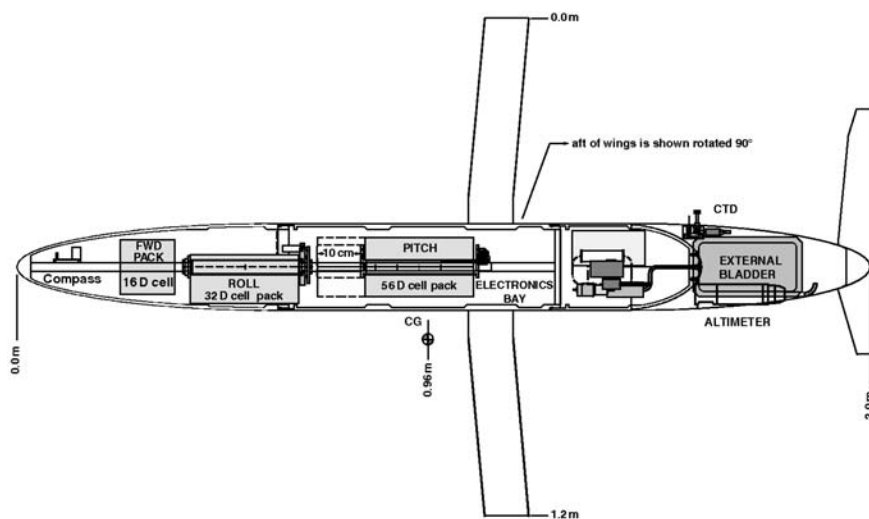


Figure 7: Diagram of the autonomous underwater glider “Spray” [22].

The design of the Spray included a study of four possible hull configurations as seen in Figure 8. The “fat” ellipsoid had a fineness ratio of approximately  $\frac{1}{3}$ , while the “slender” ellipsoid had a fineness ratio of approximately  $\frac{1}{10}$ . The four configurations were scaled based on a representative length,  $L = V^{\frac{1}{3}}$ , as depicted as a solid horizontal line in Figure 8. This allowed the hulls to be compared based on similar useful volume.

The four configurations studied in [12] were modeled and tested at various Reynolds numbers. The results were compared in Figure 9. Reynolds number was computed using the same volume-based representative length used to scale the models. At higher Reynolds numbers, it is clear that the laminar-flow shaped hull of the Seaglider is beneficial.

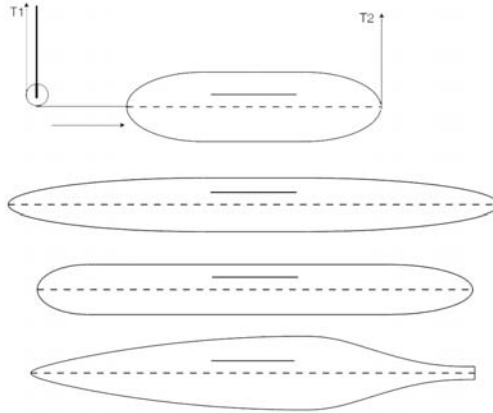


Figure 8: The four cross sections examined in [12]. From top to bottom: a “fat” ellipsoid, a “slender” ellipsoid, a cylinder with rounded ends (WRC Slocum), and a laminar flow body (UW/APL Seaglider). (Image credit: Russ Davis.)

**The Slocum Battery/Thermal.** The Slocum (thermal powered), as seen in Figure 10 was designed around the thermal stratification of the operating environment. In the warmer surface waters, the working fluid is heated and expands. This energy is accumulated and stored. In the colder waters during descent, the working fluid is cooled and is used to draw fluid out of the external reservoir. To ascend, the stored energy from heating the fluid is used to move fluid into the external reservoir, and thus creating a buoyant force. The Slocum (battery powered) was designed for shallow-water coastal operation [12]. Instead of storing thermal energy in a working fluid, the Slocum Battery uses an additional battery pack to power the ballast engine [22].

In both the Slocum Thermal and Slocum Battery, pitch control is achieved through the use of an internally actuated moving mass and the main buoyancy changer. The moving mass is used mainly for fine tuning the pitch attitude, while the majority of pitch control comes from the main buoyancy changer. To steer the vehicle, the wing is placed and designed such that rolling the vehicle results in a yawing moment. To control the roll of the vehicle, A second mass occupied approximately 180 degrees and could be rotated around the central column.

The Slocum Thermal concept has been successfully tested through several vehicles. The first, in 1995, was deployed in the Sargasso Sea on a mission to complete vertical profiling of the flow. It successfully transmitted for 240 days to depths of 1250 to 1400 m. It is unclear

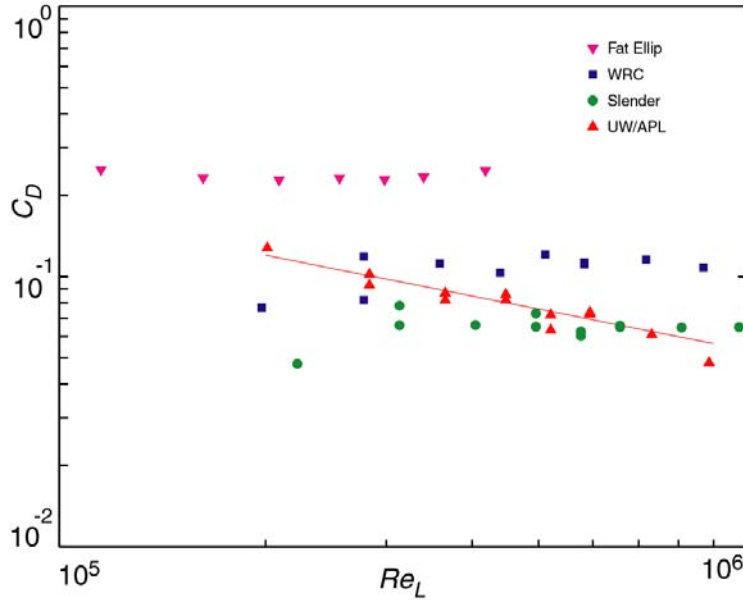


Figure 9: Measured drag of four bodies as examined in [12]. The solid line is the measured drag curve from a test using the full scale UW/APL Seaglider model. (Image credit: Russ Davis.)

why the vehicle failed, but the last known status of the vehicle showed normal operating values [12]. In 1998, in Seneca Lake, NY, a small test was conducted employing GPS to fix the location of the vehicle just before each dive and upon surfacing. The test vehicle was able to correct a heading error of 90 degrees in just 25m of depth. The 14 test dives were to a depth of 125m and ranged in glide angles from 10 to 40 degrees with horizontal speeds from 0.15 to 0.22 meters per second [12].

#### 4.2.2 Aerodynamic shape control

The SCALARS vehicle prominently features an inboard wing. This feature was mainly implemented in conjunction with the novel lateral-directional control employed by SCALARS. In [23], Spearman examines an inboard wing configuration for application in high-capacity airlift and sealift vehicles. The paper considers the possible applications of inboard wings in high-capacity airplanes, a hybrid-airship, and a wing-in-ground-effect sealift vehicle. According to the studies conducted, an inboard wing requires less structural support compared to a conventional cantilevered wing.

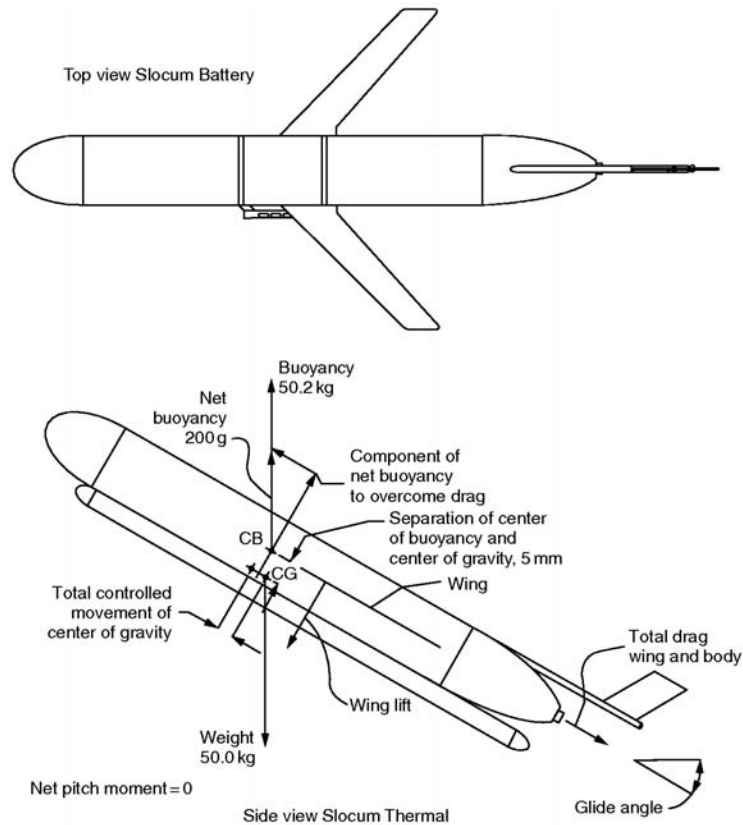


Figure 10: Diagram of the autonomous underwater glider “Slocum” [22].

In [24], Orr examines a possible design for a passenger plane featuring an inboard wing. The concept plane was able to carry more passengers without an increase in length or width. This was accomplished through increasing the chord length. The key application of this study to the SCALARS vehicle is the reduced overall length of the vehicle relative to a conventional AUV design. This fact will benefit the delivery and deployment of SCALARS.

#### 4.2.3 Autonomous Dynamic Soaring

Implementation of dynamic soaring will allow these gliders to further increase their efficiency through clever exploitation of the local wind gradient. Dynamic soaring has been demonstrated using a remotely piloted radio control aircraft in [25]. The techniques developed using the remotely piloted aircraft will be difficult to extend to autonomous vehicles. The vehicle must be able to sense a wind gradient and respond properly. Additionally, the vehicle

must be agile enough to exploit the local wind gradient.

### 4.3 Concept Development

This section describes the preliminary concept development of the SCALARS vehicle. The goal of this section is to describe the methodology used to determine initial size and performance capabilities of SCALARS. This examination uses simplistic aerodynamic estimations in order to demonstrate feasibility. Future iterations can improve upon these estimations through use of a suitable vortex lattice method (VLM) code. Currently available VLM codes are unable to process the twin-hulled, inboard wing configuration used in this design. Thus, a custom code must be developed to better analyze the aerodynamic properties and refine the size of SCALARS.

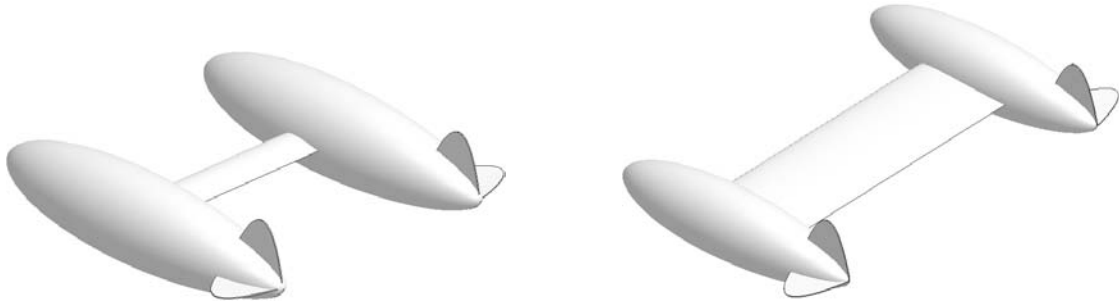


Figure 11: SCALARS Initial Concept, left, and Refined Concept, right.

The overall design of SCALARS began with the concept of the twin-hulled system to accommodate internally actuated twisting of the inboard wing. Initially, the design featured a rather small wing and empennage, as seen in Figure 11. This general concept was refined, based on the process outlined below.

#### 4.3.1 Mass

The SCALARS concept is an answer to R. D. Lorenz’s call for a “small (20-100 kg) unmanned aerial vehicle (UAV)” to follow up the Huygens mission [21]. He states that “[a] reasonable flight speed requirement would be 1 m/s, giving the ability to traverse pole to pole twice in one year (and thus, because there are east-west winds that are strong at altitude, access to

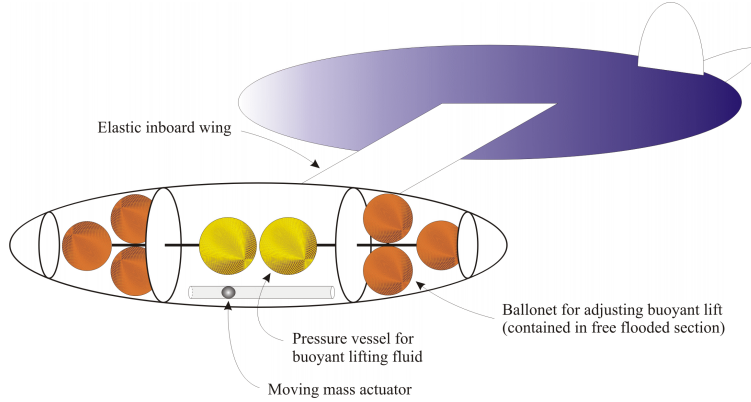


Figure 12: SCALARS internal components.

anywhere on the surface).” The SCALARS vehicles will employ a distributed sensor suite, allowing each individual SCALARS vehicle to be smaller. As a starting point, it is assumed each SCALARS has a mass of  $m = 10$  kg.

### 4.3.2 Volume

To settle on a base size for the vehicle, the outboard hulls are assumed to be prolate spheroids. Future research may employ more stream-lined hulls, to improve efficiency. However, the geometric properties scale with the assumed shape of a prolate spheroid. According to Table 1, Titan’s atmosphere has a density of  $\rho = 5.26$  kg/m<sup>3</sup>. In order to displace the assumed mass of 10 kg, the vehicle must displace

$$V = \frac{m}{\rho} = 1.9 \text{ m}^3.$$

For two prolate spheroids, each of fineness ratio  $f$ , and neglecting volume contributions by the wing and tail, we find:

$$\begin{aligned} V &= 2 \left( \frac{4}{3} \pi \left( \frac{L}{2} \right) \left( f \frac{L}{2} \right)^2 \right) \\ &= \frac{\pi}{3} f^2 L^3. \end{aligned}$$

For neutral buoyancy, each hull has a length of

$$L = \sqrt[3]{\frac{3m}{\pi\rho f^2}}.$$

In Figure 13, the length and diameter is shown for a range of fineness ratios. Selecting a fineness ratio of  $\frac{1}{4}$  provides a moderately streamlined shape, with a length of just over 3 meters, and a maximum hull diameter of approximately  $\frac{3}{4}$  meters. Major concerns for a vehicle of these dimensions are packaging and delivery. Current research into structure and materials, along with development of inflatable structures will play an important role in the development of the proposed architecture.

### 4.3.3 Lung capacity

An important parameter of buoyancy driven gliding is the lung capacity,  $\eta$ . This parameter determines the net weight change, and is driven by the required speed. The suggested speed, of 1 m/s, by Lorenz would require a prohibitively large lung. Thus a nominal speed of  $U = 0.5$  m/s was selected, which would still allow the SCALARS vehicle to make upwind progress against the expected headwinds. The necessary lung capacity is computed, for a representative example, in Section 4.3.6.

### 4.3.4 Chord length

A primary parameter in studying the flow over a vehicle is the Reynolds number, which is defined by the equation:

$$\text{Re} = \frac{\rho U l}{\mu}$$

where  $l$  is a characteristic length. According to [26], there is a crisis in the ratio of lift to drag around the Reynolds number  $10^5$ . Below this value, the lift to drag ratio severely drops, and thus it is critical to design the vehicle to glide at a higher Reynolds number. Selecting the chord length,  $c$ , as the characteristic length, and substituting given values, we require

$$c > \frac{\mu \text{Re}_c}{\rho U} = \frac{(8.051 \times 10^{-6} \text{ Pas})(10^5)}{(5.26 \text{ kg/m}^3)(0.5 \text{ m/s})} = 0.30 \text{ m}. \quad (1)$$

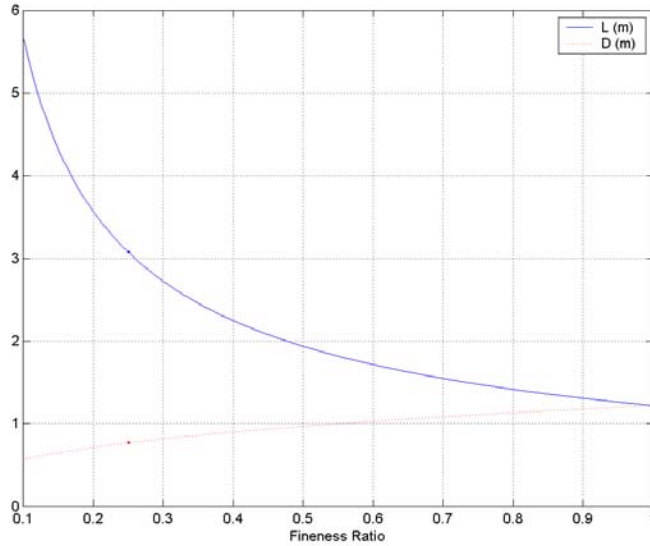


Figure 13: Hull length and diameter versus fineness ratio for  $m = 10$  kg [5].

This observation motivates the chord length selection of the representative example in Section 4.3.6. The chord length and span of the wing are important variables in determining the wing’s torsional stiffness, which determines roll control effectiveness.

### 4.3.5 Aerodynamics

**Wing contributions.** The wing is the primary contributor to the lift of the vehicle. Because SCALARS will perform both ascending and descending gliding, it is reasonable to assume that the inboard wing is symmetric. As such, the wing will produce no pitching moment about the aerodynamic center, the point at which the pitching moment does not vary with angle of attack. The lift generated by the wing is given by

$$\mathcal{L}_w = C_{\mathcal{L}_w} \left( \frac{1}{2} \rho V^2 \right) S$$

where  $\rho$  is the density of the fluid,  $V$  is the velocity of the flow, and  $S$  is the wing area. For small angles of attack, the lift coefficient takes the form

$$C_{\mathcal{L}_w} = C_{\mathcal{L}_{\alpha_w}} \alpha.$$

The lift-curve slope can be roughly approximated using the Helmbold equation [27]

$$C_{\mathcal{L}_{\alpha_w}} = \frac{\pi AR}{1 + \sqrt{1 + \left(\frac{AR}{2}\right)^2}}. \quad (2)$$

In the limit  $AR \rightarrow \infty$ , the slope of the lift curve approaches  $2\pi$ , as predicted by two-dimensional aerodynamic theory.

The lift generated by a wing increases linearly with angle of attack for small angles of attack. As the angle of attack increases beyond this range, the wing approaches stall, and loses its ability produce lift. A crude approximation for this behavior is exhibited in [5] by

$$C_{\mathcal{L}_w} = \frac{1}{2} C_{\mathcal{L}_{\alpha_w}} \sin 2\alpha.$$

The drag force acting on the wing is

$$\mathcal{D}_w = C_{\mathcal{D}_w} \left( \frac{1}{2} \rho V^2 \right) S$$

where the drag coefficient  $C_{\mathcal{D}_w}$  decomposes into the parasite and induced drag coefficients:

$$C_{\mathcal{D}_w} = C_{\mathcal{D}_{w_p}} + C_{\mathcal{D}_{w_i}}$$

The term  $C_{\mathcal{D}_{w_p}}$  includes the skin friction. An empirical approximation for the skin friction from [27] is

$$C_{\mathcal{D}_{w_p}} = \frac{0.135}{\sqrt[3]{C_f \frac{S_{w_{wet}}}{S_{w_{base}}}}} \frac{S_{w_{base}}}{S} \quad (3)$$

where  $S_{w_{base}}$  represents the area of a blunt trailing edge or the cross-sectional area of a separated flow region. For a smooth flat plate in a fully turbulent flow,

$$C_f = 0.455(\log_{10}(\text{Re}))^{-2.58}.$$

In the case of the flat plate, the wetted area is equal to twice the wing area,  $S_{w_{wet}} = 2S$ . Table 3 shows the parasite drag coefficient for a range of Reynolds numbers and base areas.

The induced drag,  $C_{\mathcal{D}_{w_i}}$ , is drag induced by the generation of lift. This coefficient can be

Table 3: Wing parasite drag coefficient  $C_{D_{w_p}}$  versus Reynolds number and base area [5].

$Re_w$	$S_{w_{base}}/S = 0.01$	$S_{w_{base}}/S = 0.05$	$S_{w_{base}}/S = 0.10$
$10^5$	0.0056	0.028	0.056
$10^6$	0.0065	0.033	0.065
$10^7$	0.0074	0.037	0.074

approximated by small angle aerodynamic theory by

$$C_{D_{w_i}} = \frac{C_{\mathcal{L}_w}^2}{\pi AR}.$$

where it is assumed that the wing loading has an elliptical distribution. Using this expression, we obtain

$$C_{D_w} = C_{D_{w_p}} + \frac{C_{\mathcal{L}_w}^2}{\pi AR}.$$

Similar to the approximation for lift, this is only applicable at small angles of attack. At large angles of attack,  $C_{\mathcal{L}_w} = 0$ , suggesting that the induced drag disappears at large angles of attack. This does not correspond to observed phenomena, and a more suitable approximation from [5] is

$$C_{D_{w_i}} = C_{D_{w_p}} + \frac{C_{\mathcal{L}_w}^2}{2\pi AR} (1 - \cos 2\alpha).$$

This approximation exhibits the expected behavior at higher angles of attack. This approximation will be used, in conjunction with the approximation for  $C_{\mathcal{L}_w}$ , to solve for optimal lift to drag ratios.

**Fuselage contributions.** The twin hulls make a large contribution to the drag of the vehicle, and a small addition to the lift. The additional lift will not change the order of magnitude solutions needed for preliminary sizing. Thus, we will neglect the lift, and focus on the drag contributions and moments due to the fuselages. The drag can be approximated by the equation for a blunt-based body [27]

$$C_{D_{hp}} = \frac{0.029}{\sqrt{C_f \frac{S_{hwet}}{S_{hbase}}}} \frac{S_{hbase}}{S}.$$

where the wetted area of a spheroidal hull is

$$S_{\text{hwet}} = 2\pi \left(\frac{L}{2}\right)^2 \left\{ f^2 + \frac{f}{\sqrt{1-f^2}} \arcsin \sqrt{1-f^2} \right\}.$$

To be conservative, we assume that separation occurs at the maximum diameter of the hull, thus obtaining

$$S_{\text{hbase}} = \pi f^2 \left(\frac{L}{2}\right)^2.$$

The total parasite drag for both hulls can thus be calculated as

$$2C_{\mathcal{D}_{\text{hp}}} = \frac{0.058\pi}{4S} (fL)^2 \left[ 2C_f \left\{ 1 + \frac{1}{f\sqrt{1-f^2}} \arcsin \sqrt{1-f^2} \right\} \right]^{-\frac{1}{2}} \quad (4)$$

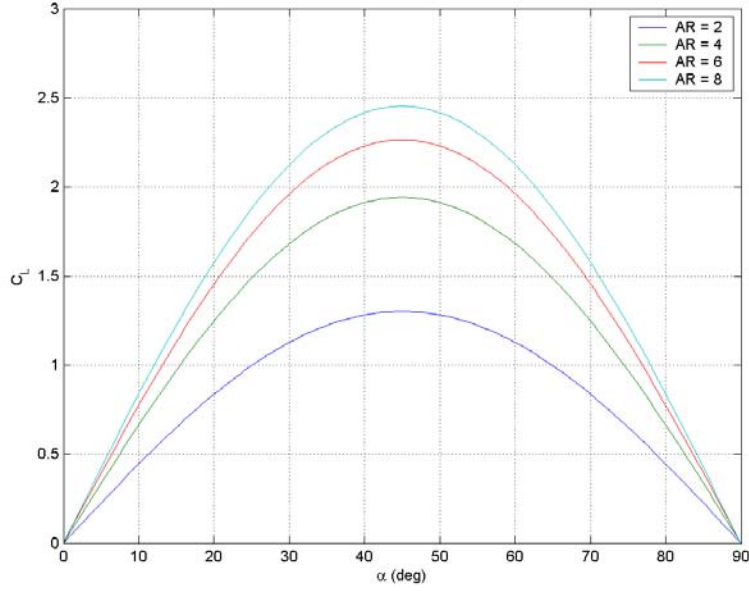


Figure 14: Vehicle lift coefficient versus angle of attack [5].

**Total aerodynamic forces.** The total aerodynamic forces on the body can therefore be written as

$$C_L = C_{L\alpha}\alpha \quad (5)$$

$$C_D = (C_{D_{wp}} + 2C_{D_{hp}}) + \frac{C_{L\alpha}^2}{2\pi AR} (1 - \cos 2\alpha) \quad (6)$$

where  $C_{L\alpha} = C_{L\alpha_w}$  is given by equation (2),  $C_{D_{wp}}$  is given by equation (3), and  $2C_{D_{hp}}$  is given by equation (4). These representations neglect the additional lift due to the body, and the lift and drag due to the empennage (the horizontal and vertical stabilizers).

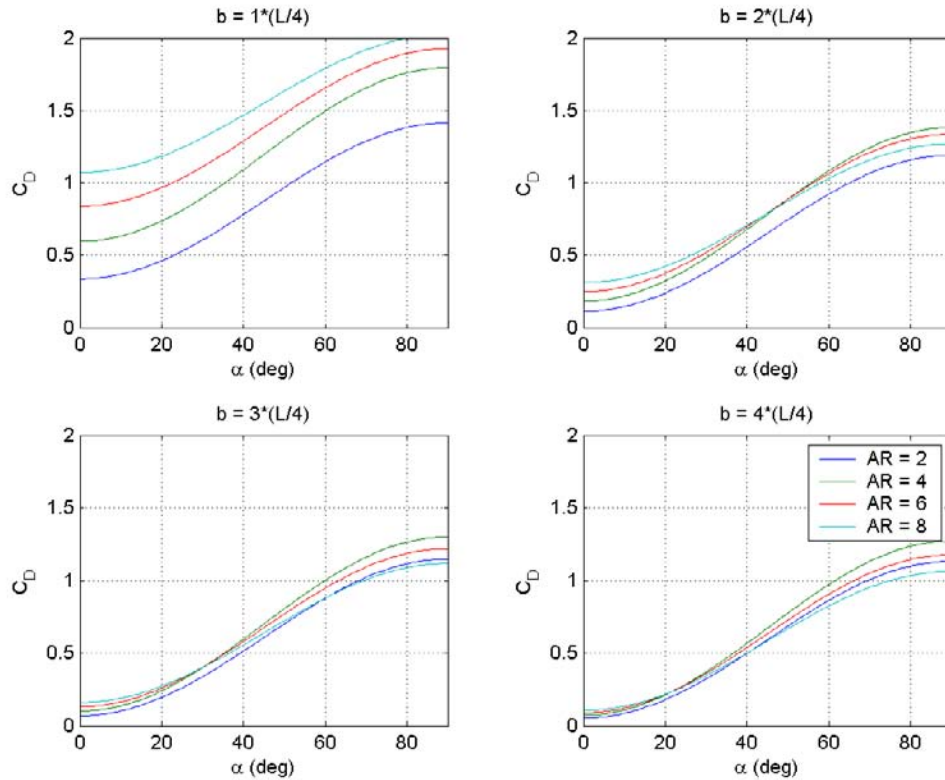


Figure 15: Vehicle drag coefficient versus angle of attack [5].

In Figure 14, from [5], the lift coefficient is shown for various values of the wing aspect ratio  $AR$ . The corresponding drag coefficient curves can be observed in Figure 15. These curves are also shown for various wing spans. These figures were created using the assumed speed of 0.5 meters per second.

The plots for drag coefficient are misleading, because the smaller wing has a smaller wing reference area. A more informative plot can be found by considering the glide path angle, as shown in Figure 16. Figure 16 shows increasing the wing span reduces the minimum glide path angle. The reduced glide path angle is drastic up to  $b = \frac{3}{4}L$ , with the benefit of moving to  $b = L$  being much less dramatic. This observation drives the selection of a wing span of  $b = \frac{3}{4}L$  for the representative example covered in Section 4.3.6.

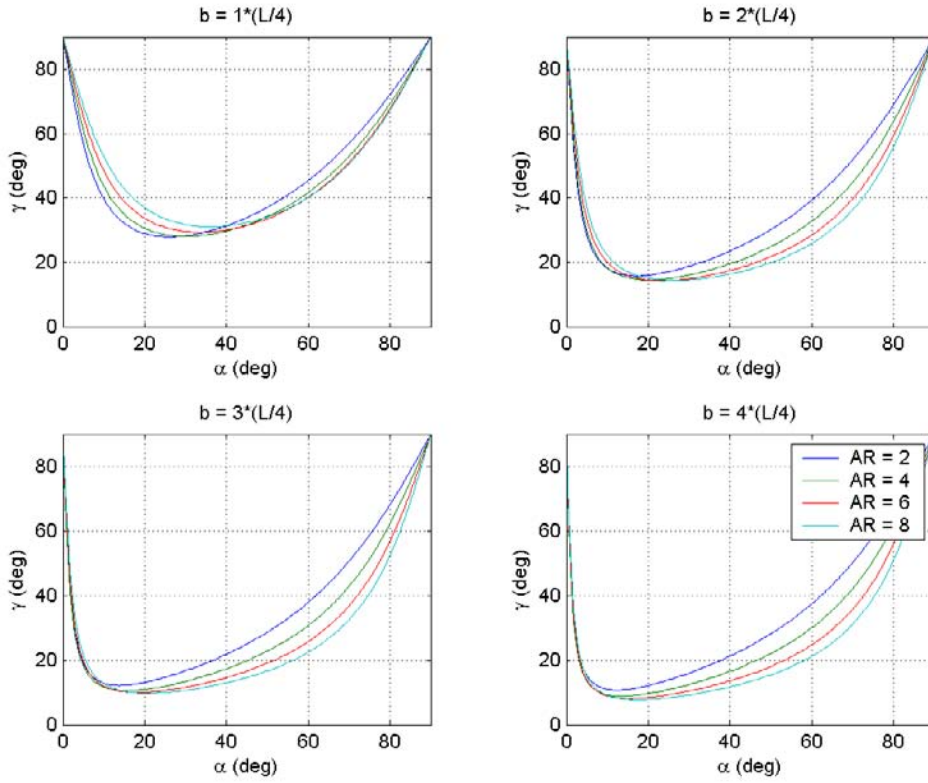


Figure 16: Glide angle versus angle of attack.

#### 4.3.6 Representative example

**Lung capacity.** Using [26], we can calculate the lung capacity

$$\eta = \frac{\rho C_D}{\Psi \sin \gamma} \left( \frac{U}{\cos \gamma} \right)^2. \quad (7)$$

We assume that the SCALARS vehicle is neutrally buoyant when the lung is half inflated, because the vehicle will operate in both descending and ascending glides. It is desirable to glide at the lowest glide path angle, maximizing horizontal distance travelled per unit of altitude. Applying this condition we obtain a lung capacity of

$$\eta = \frac{(5.26 \text{ kg/m}^3)(0.13)}{(1.9 \text{ m}^3)(0.21)} \left( \frac{0.5 \text{ m/s}}{0.98} \right)^2 = 0.45.$$

This was a motivation for selecting a slower operating speed. If the vehicle were required to fly at a speed of 1 meter per second, as suggested by Lorenz, the lung capacity would be greater than 1, and thus physically impossible.

**Aerodynamics.** Through the parametric study done above, we choose  $b = \frac{3}{4}L$  and  $AR = 2$ . These selections and the assumed speed of 0.5 meters per second allow us to calculate the Reynolds number,  $Re = 3.8 \times 10^5$ . Assuming  $S_{w_{base}} = 0.05S$ , we obtain

$$C_L = 1.30 \sin 2\alpha \quad \text{and} \quad C_D = 0.069 + 0.54(1 - \cos 2\alpha).$$

Using these solutions, we can obtain the glide path angle as a function of angle of attack, as shown in Figure 17. The minimum glide angle is approximately  $\gamma = 12^\circ$ , at an angle of attack  $\alpha = 14^\circ$ .

## 4.4 Dynamic model

### 4.4.1 Vehicle dynamics

The dynamic model for a rigid SCALARS vehicle can be determined by extending the results of [28] to include two moving masses. The effect of wing twist can be incorporated as a slight modification.

Figure 18 is a crude depiction of a SCALARS vehicle. A reference frame with orthonormal basis  $(\mathbf{I}_1, \mathbf{I}_2, \mathbf{I}_3)$  is fixed in inertial space. The body reference frame, with orthonormal basis  $(\mathbf{b}_1, \mathbf{b}_2, \mathbf{b}_3)$ , is fixed at some point in the vehicle, with  $\mathbf{b}_2$  in the direction of the right buoy and  $\mathbf{b}_3$  in the “down” direction in the plane of symmetry. The body reference frame in

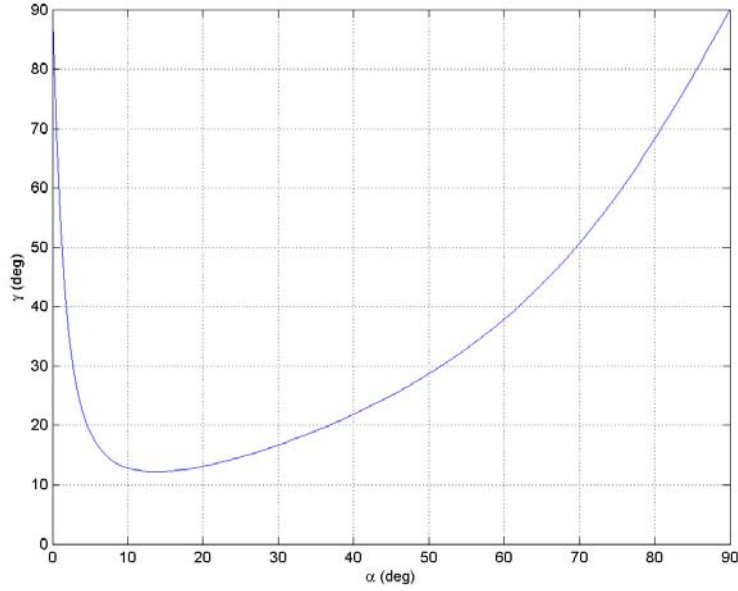


Figure 17: Glide angle versus angle of attack:  $AR = 2$  and  $b = \frac{3}{4}L$  [5].

the SCALARS vehicle differs from conventional aircraft because it is located at the center of buoyancy, which does not move, instead of the center of gravity, which moves in the SCALARS vehicle. A proper rotation matrix  $\mathcal{R}$  transforms free vectors from the body reference frame to the inertial reference frame. The inertial vector  $\mathbf{X}$  locates the origin of the body frame in inertial space.

Let the body frame vectors  $\boldsymbol{\omega}$  and  $\mathbf{v}$  represent the angular and linear velocity of the body with respect to inertial space, respectively. Next, define the operator  $\hat{\cdot}$  by requiring that  $\hat{\mathbf{a}}\mathbf{b} = \mathbf{a} \times \mathbf{b}$  for vectors  $\mathbf{a}, \mathbf{b} \in \mathbb{R}^3$ . In matrix form,

$$\hat{\mathbf{a}} = \begin{pmatrix} 0 & -a_3 & a_2 \\ a_3 & 0 & -a_1 \\ -a_2 & a_1 & 0 \end{pmatrix}.$$

The kinematic equations for the body are therefore

$$\dot{\mathcal{R}} = \mathcal{R}\hat{\boldsymbol{\omega}} \tag{8}$$

$$\dot{\mathbf{X}} = \mathcal{R}\mathbf{v} \tag{9}$$

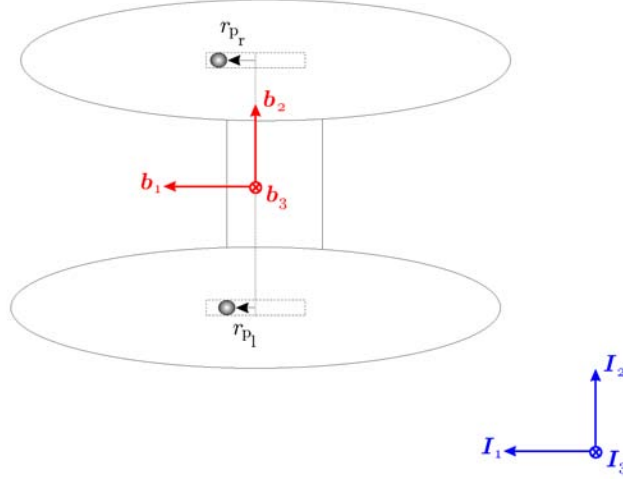


Figure 18: Illustration of reference frames and notation for SCALARS vehicle model [5].

Let the body vector  $\mathbf{v}_{p_l}$  denote the velocity of the left-side moving mass particle with respect to inertial space. The kinematic equation for this mass particle is

$$\dot{\mathbf{X}}_{p_l} = \mathcal{R}\mathbf{v}_{p_l}. \quad (10)$$

Now let the inertial vector  $\mathbf{R}_{p_l} = \mathbf{X}_{p_l} - \mathbf{X}$  denote the position of the mass particle relative to the origin of the body frame. Define the body vector  $\tilde{\mathbf{v}}_{p_l} = \mathbf{v}_{p_l} - \mathbf{v}$ . An alternative kinematic equation for the mass particle is

$$\dot{\mathbf{R}}_{p_l} = \mathcal{R}\tilde{\mathbf{v}}_{p_l}. \quad (11)$$

Finally, define  $\mathbf{r}_{p_l} = \mathcal{R}^T \mathbf{R}_{p_l}$  to be the vector  $\mathbf{R}_{p_l}$  expressed in the body frame. Differentiating, and using equations (8) - (10), gives a third kinematic equation for the mass particle

$$\begin{aligned} \dot{\mathbf{r}}_{p_l} &= \dot{\mathcal{R}}^T \mathcal{R}_{p_l} + \mathcal{R}^T (\dot{\mathbf{X}}_{p_l} - \dot{\mathbf{X}}) \\ &= -\boldsymbol{\omega} \times \mathbf{r}_{p_l} + \mathbf{v}_{p_l} - \mathbf{v}. \end{aligned} \quad (12)$$

Rearranging equation (12) gives the familiar expression for the velocity  $\mathbf{v}_{p_l}$  of a point expressed in a rotating reference frame. Because the point mass is constrained to move parallel to the vehicle's longitudinal axis, only the first component of the vector  $\mathbf{r}_{p_l}$  is free to vary under the influence of a control force. We therefore define  $r_{p_l} = \mathbf{e}_1 \cdot \mathbf{r}_{p_l}$  where  $\mathbf{e}_1 = [1, 0, 0]^T$ .

The kinematic model for the right-side moving point mass can be developed similarly.

To determine the complete vehicle dynamic equations, define the generalized inertia matrix for the body/particle system as

$$\mathbb{I}_{b/p} = \begin{pmatrix} \mathbf{J}_b - m_{p_l} \hat{\mathbf{r}}_{p_l} \hat{\mathbf{r}}_{p_l} - m_{p_r} \hat{\mathbf{r}}_{p_r} \hat{\mathbf{r}}_{p_r} & m_b \hat{\mathbf{r}}_{cg} + m_{p_l} \hat{\mathbf{r}}_{p_l} + m_{p_r} \hat{\mathbf{r}}_{p_r} & m_{p_l} \hat{\mathbf{r}}_{p_l} \mathbf{e}_1 & m_{p_r} \hat{\mathbf{r}}_{p_r} \mathbf{e}_1 \\ -m_b \hat{\mathbf{r}}_{cg} - m_{p_l} \hat{\mathbf{r}}_{p_l} - m_{p_r} \hat{\mathbf{r}}_{p_r} & m \mathbb{I}_{3 \times 3} & m_{p_l} \mathbf{e}_1 & m_{p_r} \mathbf{e}_1 \\ -m_{p_l} \mathbf{e}_1^T \hat{\mathbf{r}}_{p_l} & m_{p_l} \mathbf{e}_1^T & m_{p_l} & 0 \\ -m_{p_r} \mathbf{e}_1^T \hat{\mathbf{r}}_{p_r} & m_{p_r} \mathbf{e}_1^T & 0 & m_{p_r} \end{pmatrix}.$$

The generalized added inertia matrix (due to motion through a fluid) is

$$\mathbb{I}_f = \begin{pmatrix} \mathbf{J}_f & \mathbf{D}_f & 0 & 0 \\ \mathbf{D}_f^T & \mathbf{M}_f & 0 & 0 \\ \mathbf{0}^T & \mathbf{0}^T & 0 & 0 \\ \mathbf{0}^T & \mathbf{0}^T & 0 & 0 \end{pmatrix}.$$

The total generalized inertia matrix is defined as the sum of the body/particle system inertia and the added inertia,  $\mathbb{I}_{sys} = \mathbb{I}_{b/p} + \mathbb{I}_f$ . Next, define the total body angular momentum  $\mathbf{H}_{sys}$  and the total body translational momentum  $\mathbf{P}_{sys}$ . Also, define the longitudinal components of the moving point mass momenta  $P_{p_l}$  and  $P_{p_r}$ . The generalized momentum vector is

$$\boldsymbol{\nu} = \begin{pmatrix} \mathbf{H}_{sys} \\ \mathbf{P}_{sys} \\ P_{p_l} \\ P_{p_r} \end{pmatrix}. \quad (13)$$

Finally, define the generalized velocity vector

$$\boldsymbol{\eta} = \begin{pmatrix} \boldsymbol{\omega} \\ \mathbf{v} \\ \dot{r}_{p_l} \\ \dot{r}_{p_r} \end{pmatrix}. \quad (14)$$

The generalized velocity and momentum are related by

$$\boldsymbol{\nu} = \mathbb{I}_{sys}\boldsymbol{\eta}.$$

The  $8 \times 8$  generalized inertia matrix,  $\mathbb{I}_{sys}$ , is positive definite and depends on the vehicle geometry and mass distribution. It also includes added mass and added inertia effects which are important for airships.

The dynamic equations of motion are derived from Newton's Second Law of Motion using the equations for the angular momentum  $\mathbf{H}_{sys}$ , system linear momentum  $\mathbf{P}_{sys}$ , and point mass linear momenta  $\mathbf{P}_{pr}$  and  $\mathbf{P}_{pl}$ , as expressed in the inertial frame. The inertial and body momenta are related by the following equations:

$$\mathbf{H}_{sys} = \mathcal{R}\mathbf{h}_{sys} + \mathbf{X} \times \mathbf{p}_{sys} \quad (15)$$

$$\mathbf{P}_{sys} = \mathcal{R}\mathbf{p}_{sys} \quad (16)$$

$$\mathbf{P}_{pr} = \mathcal{R}\mathbf{p}_{pr} \quad (17)$$

$$\mathbf{P}_{pl} = \mathcal{R}\mathbf{p}_{pl} \quad (18)$$

Note that  $\mathbf{H}_{sys}$  is taken about the inertial frame origin, while  $\mathbf{h}_{sys}$  is taken about the body frame origin. To solve for the dynamic equations, the forces and moments need to be taken into account. In the inertial frame,

$$\mathcal{M}_{ext} = \dot{\mathbf{H}}_{sys} \quad (19)$$

$$\mathcal{F}_{ext} = \dot{\mathbf{P}}_{sys} \quad (20)$$

$$\mathcal{F}_{intr} = \dot{\mathbf{P}}_{pr} \quad (21)$$

$$\mathcal{F}_{int_1} = \dot{\mathbf{P}}_{pl} \quad (22)$$

Differentiating equations (15) - (16), using equations (19) - (20), and expressing the forces and moments in the body frame, we can solve for the following equations of motion. The

final equations of motion, including the kinematics (8), (9), and (12), are

$$\dot{\mathcal{R}} = \mathcal{R}\hat{\omega} \quad (23)$$

$$\dot{\mathcal{X}} = \mathcal{R}\mathbf{v} \quad (24)$$

$$\dot{\mathbf{r}}_{p_l} = -\boldsymbol{\omega} \times \mathbf{r}_{p_l} + \mathbf{v}_{p_l} - \mathbf{v} \quad (25)$$

$$\dot{\mathbf{r}}_{p_r} = -\boldsymbol{\omega} \times \mathbf{r}_{p_r} + \mathbf{v}_{p_r} - \mathbf{v} \quad (26)$$

$$\dot{\mathbf{h}}_{sys} = \hat{\mathbf{h}}_{sys}\boldsymbol{\omega} + \hat{\mathbf{p}}_{sys}\mathbf{v} + \mathcal{M} \quad (27)$$

$$\dot{\mathbf{p}}_{sys} = \hat{\mathbf{p}}_{sys}\boldsymbol{\omega} + \mathcal{F} \quad (28)$$

$$\dot{p}_{p_l} = (\hat{\mathbf{p}}_{p_l}\boldsymbol{\omega} + \mathcal{F}_{p_l}) \cdot \mathbf{e}_1 \quad (29)$$

$$\dot{p}_{p_r} = (\hat{\mathbf{p}}_{p_r}\boldsymbol{\omega} + \mathcal{F}_{p_r}) \cdot \mathbf{e}_1 \quad (30)$$

The last two equations may be replaced through a partial feedback linearization, with

$$\dot{p}_{p_l} = u_l$$

$$\dot{p}_{p_r} = u_r$$

#### 4.4.2 Equilibrium

The SCALARS vehicle will operate in equilibrium glide in the plane of symmetry throughout most of its motion. Therefore, it is important to determine the equilibria, and how the parameters affect these equilibria. Some states and inputs of interest are position of the masses  $\mathbf{r}_p$ , buoyant force  $\mathbf{B}$ , angle of attack ( $\alpha$ ), glide angle ( $\gamma$ ), and pitch angle ( $\theta$ ). As described in Figure 19, the three angles are related by the equation  $\theta = \gamma - \alpha$ , thus reducing the states on interest by one. The investigation begins by examining the state vector, expressed as both momenta and velocities, described by equations (13) - (14), respectively.

The equilibrium that we are concerned with is steady motion in the plane of symmetry, specifically, the  $x$ - $z$  plane. This motion simplifies the state vectors to  $\nu = [\mathbf{p}, \mathbf{0}, p_{p_l}, p_{p_r}]^T$  and  $\eta = [\mathbf{0}, \mathbf{v}, 0, 0]^T$ . equations(27) and (28) then become

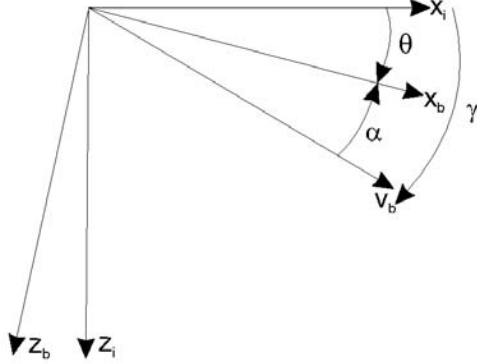


Figure 19: Angles in the plane of symmetry.

$$\mathbf{0} = \mathcal{F} \quad (31)$$

$$\mathbf{0} = \hat{\mathbf{p}}_{sys} \mathbf{v} + \mathcal{M} \quad (32)$$

An interesting note is that equation (32) simplifies down to  $\mathcal{M} = \mathbf{0}$  when the total mass matrix can be expressed as  $\mathbf{M} = m\mathbb{I}_{3 \times 3}$ . This is the case, for example, when the vehicle has a much greater density than the ambient fluid (such as an airplane in Earth's atmosphere).

Taking equation (31) in the inertial frame, and examining the forces in the horizontal direction, we obtain the following equation for glide path angle

$$\tan \gamma = \frac{\Sigma \mathcal{D}}{\Sigma \mathcal{L}} \quad (33)$$

where  $\Sigma \mathcal{D}$  is the sum of the drag of body, wing, and tail. Likewise,  $\Sigma \mathcal{L}$  is the sum of the lift of body, wing, and tail. Solving equation (31) in the gravitational direction, and substituting equation (33) solved for  $\Sigma \mathcal{D}$ , the following relation is found

$$\cos \gamma = \frac{\Sigma \mathcal{L}}{W - B} \quad (34)$$

where  $W$  is the weight of the vehicle, and  $B$  is the vehicle buoyancy. Defining the total lift as  $\Sigma \mathcal{L} = \frac{1}{2} \rho v^2 S C_{L\Sigma}$ , where  $S$  is the inboard wing area, we can use equation (34) to solve for

the velocity of the vehicle

$$v^2 = \frac{2(W - B) \cos \gamma}{\rho S C_{L\Sigma}} \quad (35)$$

The final equation for equilibria is found from equation (32). The only moments are about the out-of-plane axis. To simplify the equation, the mass matrix,  $\mathbf{M}$ , is assumed to be diagonal, with the components  $(m_1, m_2, m_3)$ . Solving for the position of the moving masses relative to the body frame and described in inertial space, we obtain the equation

$$r_{p1} = (k_1 - k_3) - (k_1 - k_2) \frac{B}{W} \quad (36)$$

where the k-values are defined as:

$$\begin{aligned} k_1 &= \frac{(m + 2m_p) \cos \gamma}{2\rho m_p S C_{L\Sigma}} (m_1 - m_3) \sin 2\alpha + k_4 \\ k_2 &= \frac{m + 2m_p}{2m_p} r_{cg1} \\ k_3 &= \frac{m}{2m_p} r_{cg1} \\ k_4 &= \left[ (C_{L_w} \cos \alpha + C_{D_w} \sin \alpha) r_{ac_w} + (C_{L_t} \cos \alpha + C_{D_t} \sin \alpha) \frac{S_t}{S} r_{ac_t} \right] \frac{\cos \gamma}{C_{L\Sigma}} \end{aligned}$$

In these expressions,  $r_{cg}$  is position of the center of gravity relative to the body frame described, and the subscript 1 denotes the first component of this vector in inertial space. For neutral buoyancy, where  $B/W$  is equal to one, the point mass will be located at  $(k_2 - k_3)$ . This location is the ratio of the mass of the vehicle to the point masses multiplied by the position of the center of gravity, so the sum of the moments is zero.

In equilibrium descent,  $B/W$  is between zero and one. In this case, it is intuitive to move the masses aft to maintain a positive angle of attack. In the case where the center of gravity coincides with the origin of the body, equation (36) simplifies to

$$r_{p1} = \left(1 - \frac{B}{W}\right) k_1 \quad (37)$$

This requires that  $k_1$  must be less than zero. Examining  $k_1$ , all the terms except  $k_4$  will be positive, if the glide path angle is within  $\pm 90$  degrees. This requires that  $k_4$  must be negative,

which puts a constraint on the design and placement of the horizontal tail. Removing the assumption that the center of gravity coincides with the body frame origin in the  $x$  inertial direction, we obtain

$$k_1 < \frac{(k_2 - k_3)}{\left(\frac{B}{W} - 1\right)}$$

Moving the center of gravity forward increases the constraint on the design and placement of the horizontal tail.

**Numerical Simulation.** With the equations of motion and equilibria determined, the system can be numerically simulated. The simulation provides some evidence concerning the stability of the system. The equations of motion were implemented in Matlab, see Appendix A, and the following parameters were used

<b>Hull</b>	<b>Wing</b>
$L = 1.9m$	$c = 3L/8$
$f = 6$	$b = 3L/4$
	$AR = 2$
<b>HorizontalTails</b>	<b>VerticalTails</b>
$c_t = 0.3m$	$c_v = 0.3m$
$b_t = 0.3m$	$b_v = 0.3m$
$AR_t = 1$	$AR_v = 1$

The numerical simulation implemented a nine degree of freedom vehicle dynamic model for the SCALARS vehicle. To numerically integrate the simulation, ODE45 in Matlab, an automatic step-size Runge-Kutta-Fehlberg integration method, was used. To account for wing twist, a static model based on wing stiffness was used. Applying a static wing twist model results in the loss of aeroelastic effects. A buoyancy engine was also included in the simulation through the use of a first order filter. To examine the system, an open loop control law was applied, with chosen maneuvers of a left hand turn, and two right hand turns. The control histories were determined through trial and error.

To complete a left hand turn, the system was simulated in an equilibrium descent, followed

by an asymmetric movement of the masses. The left mass was moved forward, while the right mass was moved back. The asynchronous mass positions results in a wing twist and the vehicle rolling, and then turning left. After completing the turn, the masses are returned to their original position, and the vehicle returns to equilibrium. This can be seen in Figure 20. The system responded as expected, suggesting that the simulated system is stable in this maneuver.

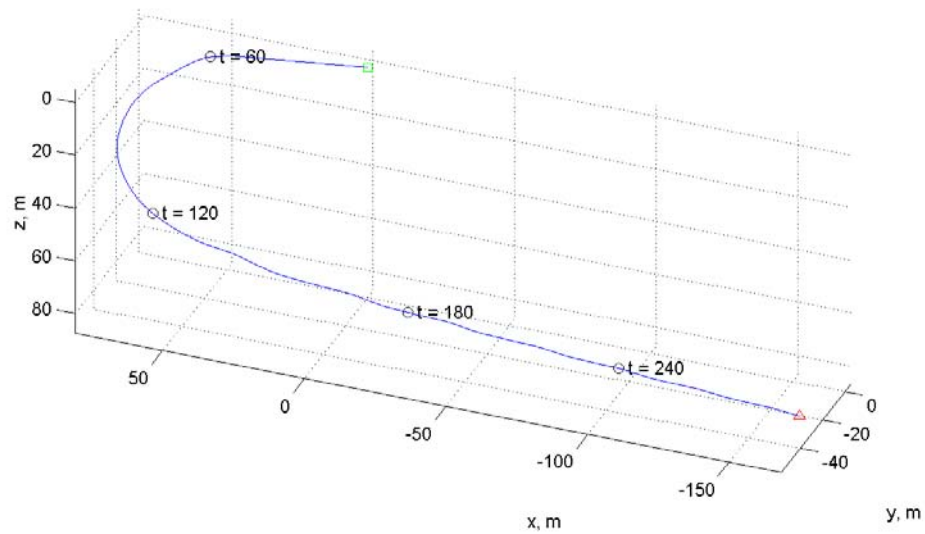


Figure 20: Flight path of SCALARS vehicle in a descending 180 degree left hand turn.

The two right hand turn maneuvers were completed similarly to the left hand turn. The vehicle was begun in equilibrium ascent, followed by an asymmetric movement of the masses. The right mass was moved forward, while the left mass was moved back. The right hand turn paths are seen in Figure 21.

Examining these glide paths, we see a “wobble” in the motion of the vehicle before returning to an equilibrium glide. A feedback control law would presumably damp these oscillations out.

## 4.5 Future Development

This section reviewed the current work done on the SCALARS vehicle. The current work is not a comprehensive treatment of the concept. Further development of the SCALARS vehicle concept should proceed through another iteration of the design procedure. Higher fidelity modeling assumptions and techniques should be used in these future iterations, including modifying an existing vortex lattice code to obtain a better aerodynamic model. Specific scientific missions and related operational hardware needed, including material selection, should be determined. Future work should also compare the SCALARS vehicle with possible competing concepts in terms of performance and energy efficiency. Finally, the analysis of stability and controllability should be refined or formalized.

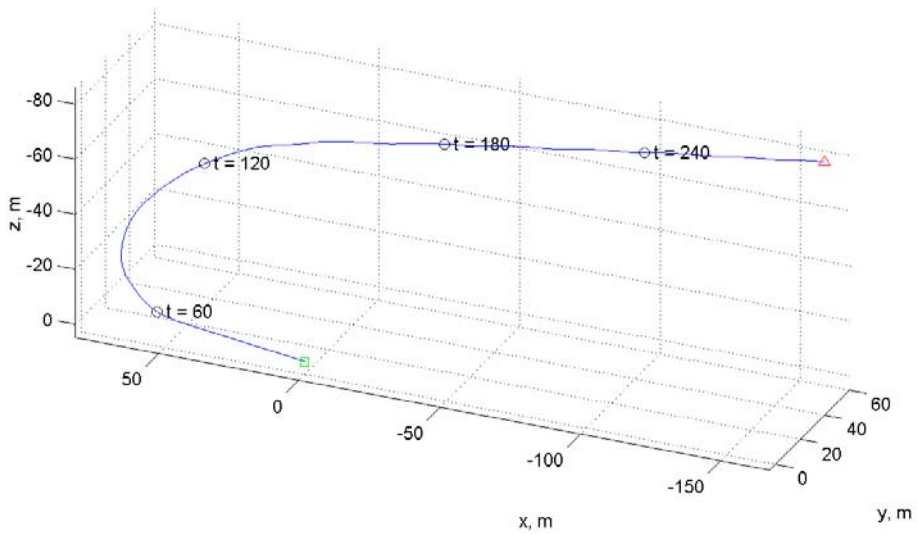
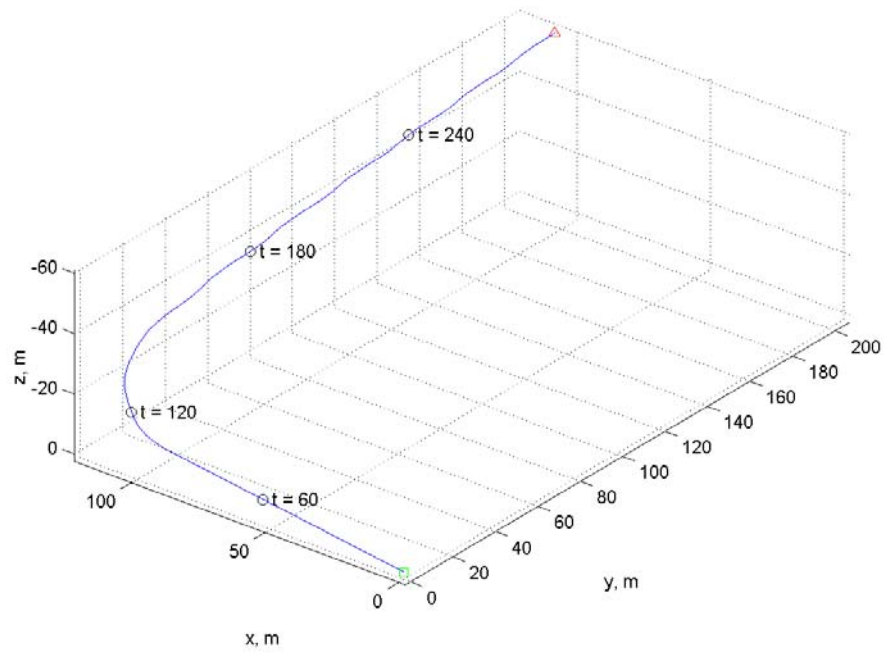


Figure 21: Flight path of SCALARS vehicle for two ascending right hand turns. The top image is of a 90 degree right hand turn. The bottom image shows a 180 degree right hand turn.

## 5 Wind Energy Absorber

This section describes the Oscillating-Aerofoil Wind Energy Absorber (OAWEA).

### 5.1 System description

The original concept for the OAWEA vehicle, as seen in Figure 22, is based off oscillating energy conversion devices that have been developed for tidal-stream energy conversion [5]. The vehicle is tethered to a mooring aerostat, which is connected to the base station. These tethers will allow energy collected by the OAWEA to be transferred to the base station, to later recharge the SCALARS vehicles. To gather energy from the ambient flow, the OAWEA vehicle employs linear induction generators.

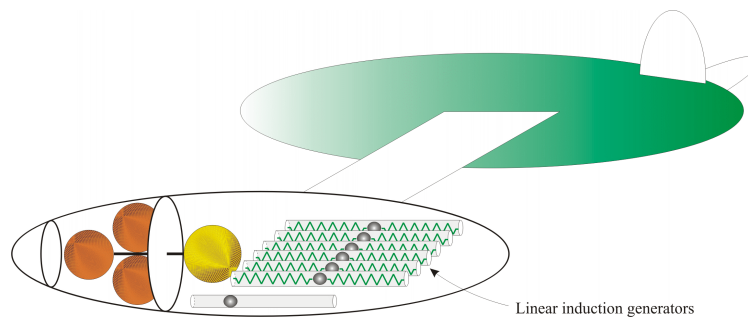


Figure 22: OAWEA internal components.

### 5.2 Representative system

The arrangement of components in the OAWEA system is similar to a two-stage towed vehicle. In [29], Schuch describes the construction of a towfish, designed to house a five-beam acoustic Doppler current profiler (VADCP), which is used to measure small-scale ocean turbulence. The towfish was designed to operate at depths up to 200 meters, regulating its attitude within 1 degree of nominal at speeds ranging from 1 to 3 meters per second.

The towfish vehicle is tethered to the research vessel, with a depressor weight attached to the cable to reduce the effect of the towing vehicle motion on the towfish. To maintain the pitch



Figure 23: A two-stage towing system [5].

requirement, the towfish fins were actuated. This arrangement can be seen in Figure 23. A numerical simulation of the towfish system was developed at Virginia Tech, providing an excellent resource to explore the OAWEA system [29]. For the OAWEA application, the two-stage towing system would be inverted, with the depressor weight being replaced by the mooring aerostat.

### 5.3 Simulation

The numerical simulation of the towfish system was examined and various design parameters (longitudinal center of gravity location, tail fin size, and pigtail length) were changed to observe the effect. The initial non-actuated configuration of the towfish resulted in a damped motion. In the OAWEA vehicle, this is undesirable, as ambient energy must drive the system's motion so to be extracted through the linear inductive generators. Through experimentation, the system was made to exhibit a self-sustaining phugoid-like oscillation, as seen in Figure 24.

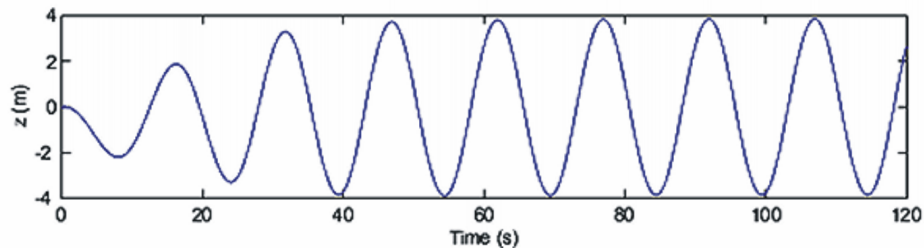


Figure 24: A limit cycle oscillation in an unstable two-stage towing system.

The motion seen in Figure 24 demonstrates a limit cycle oscillation of the vehicle. This

simulation did not include the effect of the linear inductive generators, which would extract energy from the system, acting like dampers. If the addition of these dampers results in the system exhibiting undesired properties, the design parameters of the system would have to be adjusted.

## **5.4 Future Development**

This section reviewed the investigation of the OAWEA vehicle. Future research should further modify the towed vehicle simulation, implementing the OAWEA vehicle geometry and linear inductive generators. Power generation should be investigated and compared with any competing concepts. Further information about the atmosphere on Titan will allow the design of the linear inductive generators, though knowledge of expected behavior of the OAWEA vehicle.

## 6 Extendibility to Other Operating Environments

The application of the proposed system extends to other fluid environments, including the possible methane lakes of Titan, the corrosive atmosphere of Venus, or Earth's oceans. In Table 1, some key properties of these potential operating environments are listed. These environments are discussed in more detail below.

### 6.1 Venus

Venus is an ideal environment for this system. Exploration of Venus requires a system to be highly resistant to the corrosive atmosphere, which contains sulphuric acid. This requirement benefits from an internally actuated system like SCALARS, due to moving parts being sheltered from the environment.

The atmosphere on Venus is ten times as dense as the atmosphere on Titan, greatly reducing the volume of the vehicle required for neutral buoyancy. The pressure on the surface is approximately two orders of magnitude larger than Titan, nearly equivalent to 1 km of depth in the oceans on Earth. Based on the existence of current gliders, it is reasonable to project that gliders would be able to operate in the Venusian atmosphere. The only remaining concern is the extreme temperatures on the surface.



Figure 25: Venus, as imaged by Galileo. (Image credit: NASA)

The temperatures experienced on Venus are due to the energy absorbed from the sun, even in

the presence of a dense atmosphere, which reflects much of the solar energy. This energy can be harvested through solar panels, assuming they can be engineered to survive the hostile environment. The atmospheric flows are also driven by this influx of energy, supplying the OAWEA component a suitable source of energy

## 6.2 Earth Hydrosphere

Extension of the system to the hydrosphere on Earth is quite feasible, especially considering many of the enabling technologies stem from current research concerning ocean exploration; see Figure ??, for example. The proposed system would combine current projects and improve upon them by creating a self-sustaining scientific monitoring system. The key to implementing a system that is self-sustaining is harvesting and storing energy. In the Earth's ocean, solar energy and wave energy are easily accessible. Solar energy collectors will be subject to corrosion and biological fouling, on time scales considered short for many scientific interests, and wave energy must be collected at the air-sea interface or in shallow regions [5].

## 6.3 Earth Atmosphere

There are still many scientific interests concerning the Earth's atmosphere. There are a few issues that arise when considering this system for use in Earth's atmosphere. The first concern is the fact that the atmosphere on Earth is even less dense than that on Titan, increasing the volume required for neutral buoyancy. This problem is only compounded by the atmospheric disturbances present. These concerns are key in extending the system. Lighter-than-air vehicles have been successfully used in the past, lending credibility to the possibility of applying the proposed architecture. There is also a current proposal for "efficient transportation of people and cargo" using aerial buoyancy driven gliders <sup>1</sup> [5].

---

<sup>1</sup>See <http://www.fuellessflight.com/>.



Figure 26: Earth, as imaged by Galileo. (Image credit: NASA)

## 6.4 Europa

One of Jupiter's moons, Europa, may also be a suitable application of the system. There is conjecture about what the surface of Europa conceals. As described at [nineplanets.org](http://nineplanets.org) [7]:

The images of Europa's surface strongly resemble images of sea ice on Earth. It is possible that beneath Europa's surface ice there is a layer of liquid water, perhaps as much as 50 km deep, kept liquid by tidally generated heat. If so, it would be the only place in the solar system besides Earth where liquid water exists in significant quantities.

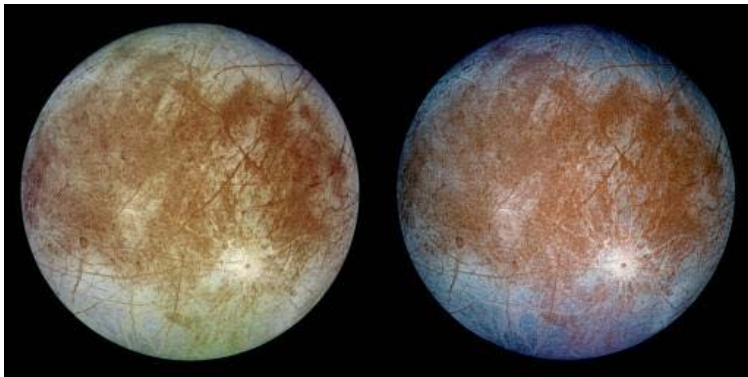


Figure 27: Europa, as imaged by Galileo. (Image credit: NASA)

If this observation leads to the discovery of liquid water in Europa, it may be possible to explore this environment with the proposed system. This could lead to the discovery of the first life form not originating from Earth. Recent discovery of ecosystems devoid of solar energy, and based entirely on chemosynthesis, lead scientists to believe life as we define it merely needs water to flourish. Discovery of life on Europa would further cement the evidence for this belief.



Figure 28: A deep-sea hydrothermal vent (left, Image credit: NASA [30]) and a colony of tubeworms (right, Image credit: NASA [31]).

Due to the nature of the exploration of Europa, several new issues arise. Delivery of the SCALARS vehicles beneath the surface becomes an additional hurdle to overcome. Once delivered, determining the position of the vehicle becomes a key concern, and communication is also vital. Vehicle positioning and communication on Europa are hurdles also present in Earth's oceans, and should be an area of research as underwater gliders become more widely distributed.

## 7 Conclusions

This thesis describes the preliminary design of a system for remote terrain exploration and environmental sampling on worlds with dense atmospheres. The motivation for the system is to provide a platform for long-term scientific studies of these celestial bodies. The proposed design is uniquely adapted to extract energy from the surrounding environment to provide a long-term platform for scientific studies. While the proposed system is novel, virtually all of the enabling technologies currently exist or are in development.

The preliminary results described in this thesis suggest that the proposed concept is feasible and fits into NASA's shifting focus from aeronautics to exploration. For the SCALARS vehicle, a nine degree of freedom vehicle dynamic model has been developed, allowing simulations to provide strong anecdotal evidence for stability and controllability. For the OAWEA vehicle, a representative system of a two-stage towed vehicle was studied. The OAWEA study illustrated energy transfer from the flow into the system.

While the work done in this thesis is not a comprehensive treatment of the concept, it lays the groundwork for future research on planetary exploration of celestial bodies with dense atmospheres. Further development of the system should proceed through another iteration of the design procedure. Higher fidelity modeling assumptions and techniques should be used in these future iterations, including modifying an existing vortex lattice code to obtain a better aerodynamic model. Specific scientific missions and related operational hardware needed should be determined. Future work should also compare the system with possible competing concepts in terms of performance, energy efficiency, and energy harvesting. Finally, delivery of the system to remote worlds should be investigated.

## References

- [1] Visionary challenges of NASA strategic enterprises for the NASA Institute for Advanced Concepts. Technical report, NASA, January 2004.
- [2] Asif Siddiqi. Exploration of the inner planets. URL: [www.centennialofflight.gov](http://www.centennialofflight.gov).
- [3] Dr. Tony Phillips. Happy anniversary, Viking lander. URL: [science.nasa.gov](http://science.nasa.gov).
- [4] R. Lorenz and J. Mitton. *Lifting Titan's Veil*. Cambridge University Press, New York, NY, 2002.
- [5] C. Woolsey, G. Hagerman, and M. Morrow. A self-sustaining, boundary-layer-adapted system for terrain exploration and environmental sampling. NIAC Phase I Final Report, 2005.
- [6] R. D. Lorenz. Post-Cassini exploration of Titan: Science rationale and mission concepts. *Journal of the British Interplanetary Society*, 53:218–234, 2000.
- [7] B. Amett. The nine planets: A multimedia tour of the solar system. URL: [www.nineplanets.org](http://www.nineplanets.org).
- [8] S. W. Bougher, D. M. Hunten, and R. J. Phillips, editors. *Venus II*. University of Arizona Press, Tucson, AZ, 1997.
- [9] S. M. Ehlers and T. A. Weisshaar. Static aeroelastic control of an adaptive lifting surface. *Journal of Aircraft*, 30(4):534–540, 1993.
- [10] B. Sanders, F. E. Eastep, and E. Forster. Aerodynamic and aeroelastic characteristics of wings with conformal control surfaces for morphing aircraft. *Journal of Aircraft*, 40(1):94–99, 2003.
- [11] C. C. Eriksen, T. J. Osse, R. D. Light, T. Wen, T. W. Lehman, P. L. Sabin, J. W. Ballard, and A. M. Chiodi. Seaglider: A long-range autonomous underwater vehicle for oceanographic research. *Journal of Oceanic Engineering*, 26(4):424–436, 2001. Special Issue on Autonomous Ocean-Sampling Networks.

- [12] J. Sherman, R. E. Davis, W. B. Owens, and J. Valdes. The autonomous underwater glider “Spray”. *Journal of Oceanic Engineering*, 26(4):437–446, 2001. Special Issue on Autonomous Ocean-Sampling Networks.
- [13] D. C. Webb, P. J. Simonetti, and C. P. Jones. SLOCUM: An underwater glider propelled by environmental energy. *Journal of Oceanic Engineering*, 26(4):447–452, 2001. Special Issue on Autonomous Ocean-Sampling Networks.
- [14] J. G. Graver, J. Liu, C. A. Woolsey, and N. E. Leonard. Design and analysis of an underwater glider for controlled gliding. In *Conference on Information Sciences and Systems*, pages 801–806, 1998.
- [15] N. E. Leonard and J. G. Graver. Model-based feedback control of autonomous underwater gliders. *Journal of Oceanic Engineering*, 26(4):633–645, 2001. Special Issue on Autonomous Ocean-Sampling Networks.
- [16] J. G. Graver. *Underwater Gliders: Dynamics, Control, and Design*. PhD thesis, Princeton University, 2005.
- [17] S. A. Shaffer, D. P. Costa, and H. Weimerskirch. Behavioural factors affecting foraging effort of breeding wandering albatrosses. *Journal of Animal Ecology*, 70:864–874, 2001.
- [18] L. A. Young, E. W. Aiken, V. Gulick, R. Manicinelli, and G.A. Briggs. Rotorcraft as Mars scouts. In *2002 IEEE Aerospace Conference*, Big Sky, MT, 2002.
- [19] S. Vogel. *Life in Moving Fluids: The Physical Biology of Flow*. Princeton University Press, second edition, 1994.
- [20] Joseph A. Schetz. *Boundary Layer Analysis*. Prentice Hall, Upper Saddle River, New Jersey, 1993.
- [21] R. D. Lorenz. Flight power scaling of airplanes, airships, and helicopters: Application to planetary exploration. *Journal of Aircraft*, 38(2):208–214, 2001.
- [22] R. E. Davis, C. C. Eriksen, and C. P. Jones. Autonomous buoyancy-driven underwater gliders. In G. Griffiths, editor, *Technology and Applications of Autonomous Underwater Vehicles*, volume 2, chapter 3. Taylor and Francis, 2002.

- [23] M. Leroy Spearman. An inboard-wing arrangement for high-capacity airlift and sealift vehicles. Technical report, NASA Langley Research Center, 2003.
- [24] Matthew W. Orr. Aerodynamic properties of the inboard wing concept. Master's thesis, Virginia Polytechnic Institute and State University, 2000.
- [25] M. B. E. Boslough. Autonomous dynamic soaring platform for distributed mobile sensor arrays. Technical Report SAND2002-1896, Sandia National Laboratory, Albuquerque, NM, June 2002. Unlimited release.
- [26] S. A. Jenkins, D. E. Humphreys, J. Sherman, J. Osse, C. Jones, N. Leonard, J. Graver, R. Bachmayer, T. Clem, P. Carroll, P. Davis, J. Berry, P. Worley, and J. Wasyl. Underwater glider system study. Tech. Rep., Office of Naval Research, 2003.
- [27] R. F. Stengel. *Flight Dynamics*. Princeton University Press, Princeton, NJ, 2004.
- [28] C. A. Woolsey. Reduced Hamiltonian dynamics for a rigid body/mass particle system. *Journal of Guidance, Control, and Dynamics*, 28(1):131–138, 2005.
- [29] E. M. Schuch. Towfish design, simulation and control. Master's thesis, Virginia Polytechnic Institute & State University, 2004.
- [30] Becky Bray. A deep sea expedition. URL: <http://liftoff.msfc.nasa.gov/news/2001/news-thermalvent.asp>.
- [31] Kathleen Crane. In search of heat: A brief history of the search for hydrothermal vents on the deep seafloor. URL: <http://oceanexplorer.noaa.gov/explorations/02galapagos/background/history/history.html>.

# Appendix A: SCALARS Simulation Code

## Simulation Setup

```
close all clear clc

global a b JG S AR e CD0 CD1 xac St ARt CD0t CD1t xtl xtr Sv ARv
CD0v CD1v xvl xvr I e1 e2 e3 Ib mp mb mbuoy rpy rpz rcg rho g td
tb mbuoydes

td = 0; tb = 60; mbuoydes = 1;

I = eye(3); e1 = I(:,1); e2 = I(:,2); e3 = I(:,3);

L = 1.9; AR = 2;
b = L*3/4*1/2; % m - half span
a = b/AR; % m - half chord
xac = [.1;0;0];

JG = 11; S = 4*a*b; AR = (2*b)^2/S; e = 1; CD0 = 0.02; CD1 = 1.5;

% horizontal tails
at = .3; bt = .3; St = at*bt; ARt = bt^2/St; CD0t = CD0; CD1t =
CD1;
xtl = [-.9;-b;0]; %m
xtr = [-.9;b;0]; %m

% vertical tails
av = .5; bv = .5; Sv = av*bv; ARv = bv^2/Sv; CD0v = CD0; CD1v =
2.3;
xvl = [-.9;0;0]; %m
xvr = [-.9;0;0]; %m
```

```

% Point Masses
mp = 1; % kg - mass of moving masses
rpy = b; rpz = 0.0;

% Body
mb = 8; % kg - mass of body
rcg = [0;0;.02]; rcb = [0;0;0];

% Environment
g = 1.35; % m/s^2
rho = 5.26; % kg/m^3 - density
Ib = diag([1/3*b^2*mb,1/3*a^2*mb,1/3*(a^2+b^2)*mb]);

% Equilibrium
% LHT
x0 = [0; 0.1540276677; 0; 10.0456321197; 0; 0.3558946648;
-0.0199653389; 0.9537896317; -0.0199653389; 0.9537896317;
0.9969023937; 0; 0.0786422105; 0; 1; 0; -0.0786422105; 0;
0.9969023937; 0; 0; 0; 9.5000000011; ];
% RHT
%x0 = [0; 0.1421500056; 0; 9.2557804977; 0; -0.3858734026;
0.0199804555; 0.8787965955; 0.0199804555; 0.8787965955;
0.9966942814; 0; -0.0812391564; 0; 1; 0; 0.0812391564; 0;
0.9966942814; 0; 0; 0; 10.4999998470; ];

% Run EOM
t_final = 300; % Define the simulation length.
options = odeset('RelTol',1e-9); [t,x] =
ode45('NIACeomtwistLHT',[0:.1:t_final]',x0,options);

figure(1)

```

```

t1 =length(t);
xb = x(:,20);
yb = x(:,21);
zb = x(:,22);
for i = 1:length(x(:,1))
    xp(i) = [1,0,0]*[x(i,11:13)',x(i,14:16)',x(i,17:19)']*
            [x(i,7);0;0]+x(i,20);
end
tstep = 60;
tpoint = 0;
pointlist = [];
tlist = [];
while tpoint < t_final
    tpoint = tpoint + tstep;
    points = find(t>tpoint);
    if length(points) > 0
        point = points(1);
        pointlist = [pointlist,point];
        tlist = [tlist,tpoint];
    end
end
plot3(xb,yb,zb); hold on
grid on
plot3(xb(1),yb(1),zb(1),'gs')
plot3(xb(t1),yb(t1),zb(t1),'r^')
for j = 1:length(pointlist)
    plot3(xb(pointlist(j)),yb(pointlist(j)),zb(pointlist(j)),'ko')
    timestring = [' t = ',num2str(tlist(j))];
    text(xb(pointlist(j)),yb(pointlist(j)),zb(pointlist(j)),timestring)
end
%plot3(xp,-yb,-zb,'r')
range=axis;

```

```

if range(1)>-.1; range(1)=-.1; end
if range(3)>-.1; range(3)=-.1; end
if range(5)>-.1; range(5)=-.1; end
if range(2)<.1; range(2)=.1; end
if range(4)<.1; range(4)=.1; end
if range(6)<.1; range(6)=.1; end
axis(range);

xlabel('x, m')
ylabel('y, m')
zlabel('z, m')

axis equal tight
set(gca,'XDir','default', 'YDir','reverse','ZDir','reverse')
range=axis;

xchange = (range(2)-range(1))*0.02;
ychange = (range(2)-range(1))*0.02;
zchange = (range(2)-range(1))*0.02;

range = range + [-xchange,xchange,-ychange,ychange,-zchange,zchange];
axis(range);

figure(3)
subplot(2,2,1); plot(xb,-yb); xlabel('x'); ylabel('-y');
title('Top'); grid on; axis(range([1:2,3:4])); hold on
subplot(2,2,1); plot(xp,-yb,'r'); xlabel('x'); ylabel('-y');
title('Top'); grid on; axis(range([1:2,3:4])); hold on
subplot(2,2,2); plot(xb,-zb); xlabel('x'); ylabel('-z');
title('Side'); grid on; axis(range([1:2,5:6])); hold on
subplot(2,2,3); plot(-yb,-zb); xlabel('-y'); ylabel('-z');
title('Front'); grid on; axis(range([3:4,5:6])); hold on

```

## Simulation Code

```
function xdot = NIACeom(t,x)

global a b JG S AR e CD0 CD1 xac St ARt CD0t CD1t xtl xtr Sv ARv
CD0v CD1v xvl xvr I e1 e2 e3 Ib mp mb mbuoy rpy rpz rcg rho g td
tb mbuoydes

% States
Pi = x(1:3);
P = x(4:6);
rpl = [x(7);-rpy;rpz];
Ppl = x(8);
rpr = [x(9);rpy;rpz];
Ppr = x(10);
R = [x(11:13),x(14:16),x(17:19)];
xb = x(20:22);
mbuoy = x(23);

% Rotation Matrix
RT = transpose(R);

% Inertia
Inertiabm = [
    Ib-mp*hat(rpl)^2-mp*hat(rpr)^2,          mb*hat(rcg)+mp*hat(rpl)
    +mp*hat(rpr),          mp*hat(rpl)*e1, mp*hat(rpr)*e1;

    -mb*hat(rcg)-mp*hat(rpl)-mp*hat(rpr), (mb+2*mp)*eye(3),
    mp*e1,          mp*e1;
```

```

    -mp*transpose(e1)*hat(rp1),      mp*transpose(e1),
    mp,                               0;

    -mp*transpose(e1)*hat(rpr),      mp*transpose(e1),
    0,                               mp;
];
Inertiaf = diag([0,0,pi*rho*b^2,1/8*pi*rho*b^4,0,0,0,0]);
Inertia = Inertiabm + Inertiaf; invInertia = inv(Inertia);

% Find States and Velocity Vectors
States = [Pi; P; Ppl; Ppr];
Velocity = invInertia*States;
Omega = Velocity(1:3);
v = Velocity(4:6);
rpldot = Velocity(7);
rprdot = Velocity(8);

% Determine Angle of Attack (rad)
alpha = atan2(v(3),v(1));

% Determine Side Slip (rad)
beta = atan2(v(2),v(1));

Torque = [0,1,0]*mp*(hat(rp1)-hat(rpr))*RT*[0;0;1];
theta = Torque*(2*b)/JG;

% Lift/Drag of wing
CLw = pi*sin(2*alpha);
Lw = 1/2*rho*norm(v)^2*S*CLw;
CDw = CD0+CD1*(1-cos(2*alpha));
Dw = 1/2*rho*norm(v)^2*S*CDw;

```

```

% Lift/Drag of horizontal tail (Left)
CLt1 = pi*sin(2*(alpha+theta/2));
Ltl = 1/2*rho*norm(v)^2*St*CLt1;
CDt1 = CD0t+CD1t*(1-cos(2*(alpha+theta/2)));
Dtl = 1/2*rho*norm(v)^2*St*CDt1;

% Lift/Drag of horizontal tail (Right)
CLtr = pi*sin(2*(alpha-theta/2));
Ltr = 1/2*rho*norm(v)^2*St*CLtr;
CDtr = CD0t+CD1t*(1-cos(2*(alpha-theta/2)));
Dtr = 1/2*rho*norm(v)^2*St*CDtr;

% Lift/Drag of vertical tail
CLv = pi*sin(2*beta);
Lv = 1/2*rho*norm(v)^2*Sv*CLv;
CDv = CD0v+CD1v*(1-cos(2*beta));
Dv = 1/2*rho*norm(v)^2*Sv*CDv;

% Rotation -beta about z, alpha about y
Raero = [ cos(alpha)*cos(beta), -cos(alpha)*sin(beta),
          -sin(alpha);
          sin(beta),           cos(beta),           0;
          sin(alpha)*cos(beta), -sin(alpha)*sin(beta), cos(alpha)];

% Aero Forces
Faero = [ -Dw-Dtl-Dtr-2*Dv;
          -2*Lv;
          -Lw-Ltl-Ltr;];
Fb = Raero*Faero;

% Aero Moments
Mt1 = hat(xt1)*Raero*[-Dtl;0;-Ltl];

```

```

Mtr = hat(xtr)*Raero*[-Dtr;0;-Ltr];
Mt = hat(xtl)*Raero*[-Dtl;0;-Ltl]+hat(xtr)*Raero*[-Dtr;0;-Ltr];
Mv = hat(xvl)*Raero*[-Dv;-Lv;0]+hat(xvr)*Raero*[-Dv;-Lv;0];
Mw = hat(xac)*Raero*[-Dw;0;-Lw];
% Gravitational Forces/moments
Fm = (mb+2*mp-mbuoy)*g*RT*[0;0;1];
Mcg = mb*hat(rcg)*RT*[0;0;1];
Mp = mp*(hat(rpl)+hat(rpr))*RT*[0;0;1];

% Ignore the case where theta^2 is small
% because it's in the denominator
if abs(theta) > 10^-6
    CMtwist = [-1/2*pi*b*(-2*sin(theta)*cos(alpha)^2+sin(theta)+
                2*theta*cos(theta)*cos(alpha)^2-
                theta*cos(theta))/theta^2
              0;
              CD1*b*sin(alpha)*cos(alpha)*(-sin(theta)+
              theta*cos(theta))/theta^2;];
else
    CMtwist = [0;0;0];
end

Mtwist = CMtwist * 1/2*rho*norm(v)^2*S*b;

% Sum Forces/Moments
Fext = Fm + Fb; Mext = Mt + Mv + Mw + Mcg + Mp + Mtwist;

% EOM
Rdot = R*hat(Omega); xbdot = R*v; Pdot = hat(P)*Omega + Fext;
Pidot = hat(Pi)*Omega + hat(P)*v + Mext;

% Determine Ppdot

```

```

rpldotv = [rpldot;0;0]; rprdotv = [rprdot;0;0];

Inertiadot = mp*[
    -(hat(rpl)*hat(rpldotv)+hat(rpldotv)*hat(rpl)+hat(rpr)*hat(rprdotv)+
    hat(rprdotv)*hat(rpr)), hat(rpldotv)+hat(rprdotv),
    hat(rpldotv)*e1, hat(rprdotv)*e1;
    -(hat(rpldotv)+hat(rprdotv)),zeros(3,5),
    transpose(e1)*hat(rpldotv),zeros(1,5)
    transpose(e1)*hat(rprdotv),zeros(1,5)
];

invInertiadot = invInertia*Inertiadot*invInertia;

% Maneuver Vehicle
error = 10^-4;
if (t > 0) & (t < 50) % Move masses back
    mbuoydes = 0.95;
    if (rpr(1)+0.02)> error;    rprdotdes = -1;
    elseif (rpr(1)+0.02)< -error; rprdotdes = 1;
    else;                      rprdotdes = 0;
    end

    if (rpl(1)+0.02)> error;    rpldotdes = -1;
    elseif (rpl(1)+0.02)< -error; rpldotdes = 1;
    else;                      rpldotdes = 0;
    end
elseif (t > 50) & (t < 125) % Move masses asymmetrically
    mbuoydes = 0.95;
    if (rpr(1)+0.21)> error;    rprdotdes = -1;
    elseif (rpr(1)+0.21)< -error; rprdotdes = 1;
    else;                      rprdotdes = 0;
    end
end

```

```

    if (rpl(1)-0.21)> error;    rpldotdes = -1;
    elseif (rpl(1)-0.21)< -error; rpldotdes = 1;
    else;                      rpldotdes = 0;
    end
elseif (t > 125) & (t < 300) % Move masses back
    mbuoydes = 0.95;
    if (rpr(1)+0.02)> error;    rprdotdes = -1;
    elseif (rpr(1)+0.02)< -error; rprdotdes = 1;
    else;                      rprdotdes = 0;
    end

    if (rpl(1)+0.02)> error;    rpldotdes = -1;
    elseif (rpl(1)+0.02)< -error; rpldotdes = 1;
    else;                      rpldotdes = 0;
    end
else                                % Center Masses
    if rpr(1)> error;           rprdotdes = -1;
    elseif rpr(1)< -error;     rprdotdes = 1;
    else;                     rprdotdes = 0;
    end

    if rpl(1)> error;           rpldotdes = -1;
    elseif rpl(1)< -error;     rpldotdes = 1;
    else;                     rpldotdes = 0;
    end
end

%[left, right] point mass acceleration
w = ([rpldotdes;rprdotdes]-[rpldot;rprdot]);

%solving for Ppldot and Pprdot

```

```

Ab = Inertia(1:6,1:6); Bb = Inertia(1:6,7:8); Cb =
Inertia(7:8,1:6); Db = Inertia(7:8,7:8); E =
[-ones(6,1);zeros(2,1)].*(Inertia * invInertiadot*States);

Prefix = [Ab,zeros(6,2);-Cb,eye(2)]; RHS =
E+[eye(6,6);zeros(2,6)]*[Pidot; Pdot]+[-Bb;Db]*w;

% LHS = [vb_dot;omega_dot;Ppldot;Pprdot]
LHS = Prefix^-1*RHS;

Ppldot = LHS(7); Pprdot = LHS(8);

mbuoydot = .05*((mb + 2*mp)*mbuoydes-mbuoy);

% Define Output
xdot = [
    Pidot;
    Pdot;
    rpldot;
    Ppldot;
    rprdot;
    Pprdot;
    Rdot(:,1);
    Rdot(:,2);
    Rdot(:,3);
    xbdot;
    mbuoydot;
];

%% Test/Graphical Output:
%figure(10); plot(t,alpha*180/pi,'r^'); hold on
%plot(t,beta*180/pi,'b*');

```

```

if t>td+.1
    %% Test/Graphical Output:
    figure(10); plot(t,alpha*180/pi,'r^'); hold on
    plot(t,beta*180/pi,'b*');
    td=td+.1;
    fprintf('%4.4f\n',t)
% fprintf(' Fext  %4.4f  %4.4f  %4.4f\n',Fext(1),Fext(2),Fext(3))
% fprintf(' Fm  %4.4f  %4.4f  %4.4f\n',Fm(1),Fm(2),Fm(3))
% fprintf(' Faero  %4.4f  %4.4f  %4.4f\n',Faero(1),Faero(2),Faero(3))
% fprintf(' Fb  %4.4f  %4.4f  %4.4f\n',Fb(1),Fb(2),Fb(3))
% fprintf(' Mext  %4.4f  %4.4f  %4.4f\n',Mext(1),Mext(2),Mext(3))
% fprintf(' Mw  %4.4f  %4.4f  %4.4f\n',Mw(1),Mw(2),Mw(3))
% fprintf(' Mt  %4.4f  %4.4f  %4.4f\n',Mt(1),Mt(2),Mt(3))
% fprintf('  Mtr  %4.4f  %4.4f  %4.4f\n',Mtr(1),Mtr(2),Mtr(3))
% fprintf('  Mtl  %4.4f  %4.4f  %4.4f\n',Mtl(1),Mtl(2),Mtl(3))
% fprintf(' Mv  %4.4f  %4.4f  %4.4f\n',Mv(1),Mv(2),Mv(3))
% fprintf(' Mcg  %4.4f  %4.4f  %4.4f\n',Mcg(1),Mcg(2),Mcg(3))
% fprintf(' Mtwist %4.4f  %4.4f  %4.4f\n',Mtwist(1),Mtwist(2),Mtwist(3))
% va = transpose(Raero)*v;
% fprintf(' |v|-v1aero %e \n ',norm(v)-va(1))
% fprintf(' v  %4.4e  %4.4e  %4.4e\n',v(1),v(2),v(3))
% fprintf(' xbdot %4.4e  %4.4e  %4.4e\n',xbd(1),xbd(2),xbd(3))
% fprintf(' alpha =  %0.0f\n',alpha*180/pi)
% fprintf(' beta  =  %0.0f\n',beta*180/pi)
% fprintf(' theta =  %0.2f\n',theta*180/pi)
% fprintf(' CLw  =  %4.4f \n',CLw)
% fprintf(' rpr  =  %4.4e\n',rpr(1))
% fprintf(' rpl  =  %4.4e\n',rpl(1))
% fprintf(' mbuoydes =  %4.4e\n',mbuoydes)
% fprintf(' mbuoydot =  %4.4e\n',mbuoydot)
% fprintf(' rpldot =  %4.4e\n',rpldot)

```

```

% fprintf(' rprdot = %4.4e\n',rprdot)
% fprintf(' Ppldot = %4.4e\n',Ppldot)
% fprintf(' Pprdot = %4.4e\n',Pprdot)
% fprintf(' Ppl = %4.4e\n',Ppl)
% fprintf(' Ppr = %4.4e\n',Ppr)
% fprintf(' Lv(CLv)   %4.4f(%4.4f) \n',Lv,CLv)
% fprintf(' Dv(CDv)   %4.4f(%4.4f) \n',Dv,CDv)
%
% figure(11);
% vxz = sqrt(v(1)^2+v(3)^2);
% vxy = sqrt(v(1)^2+v(2)^2);
% subplot(1,2,1); plot([0,v(1)/vxz],[0,-v(3)/vxz]);
%   xlabel('x'); ylabel('-z'); axis([-1,1,-1,1])
% subplot(1,2,2); plot([0,v(1)/vxy],[0,v(2)/vxy]);
%   xlabel('x'); ylabel('y'); axis([-1,1,-1,1])
%
% fprintf(' det(R) = %5.10f\n',det(R))
% fprintf('\n')
% fprintf('R:')
% disp(R)
% fprintf('\n')
% fprintf('R*R^T:')
% disp(R*RT)
% fprintf('\n\n')
end

```

## Vita

Michael Thomas Morrow was born May 6, 1981 to Charles and Katherine Morrow. Interest in math and science led him to enroll in the Engineering department at Virginia Polytechnic Institute and State University in the Fall of 1999. Mike received his Bachelor of Science in Aerospace Engineering on May 10, 2003. His interest in dynamics and control led him to enroll in graduate school at Virginia Tech for his Master of Science in Aerospace Engineering. Upon graduation, he plans to pursue employment in the field of dynamics and control.